



Australian Government
Bureau of Meteorology

The Centre for Australian Weather and Climate Research
A partnership between CSIRO and the Bureau of Meteorology



CAWCR Research Letters

Issue 7, December 2011

P.A. Sandery, T. Leeuwenburg, G. Wang, A.J. Hollis, K.A. Day (editors)



www.cawcr.gov.au



ISSN: 1836-5949

Series: Research Letters (The Centre for Australian Weather and Climate Research); Issue 7.

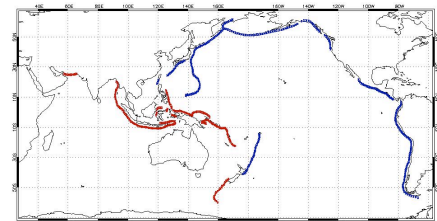
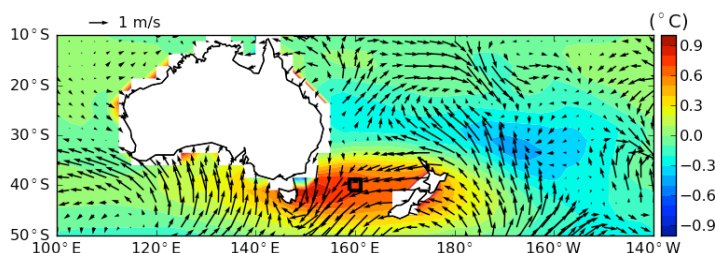
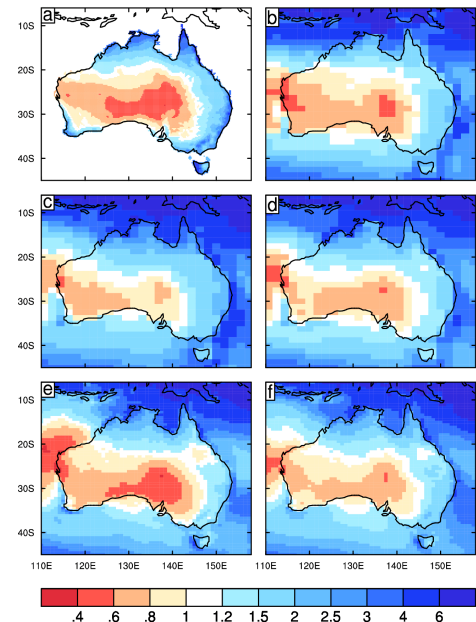
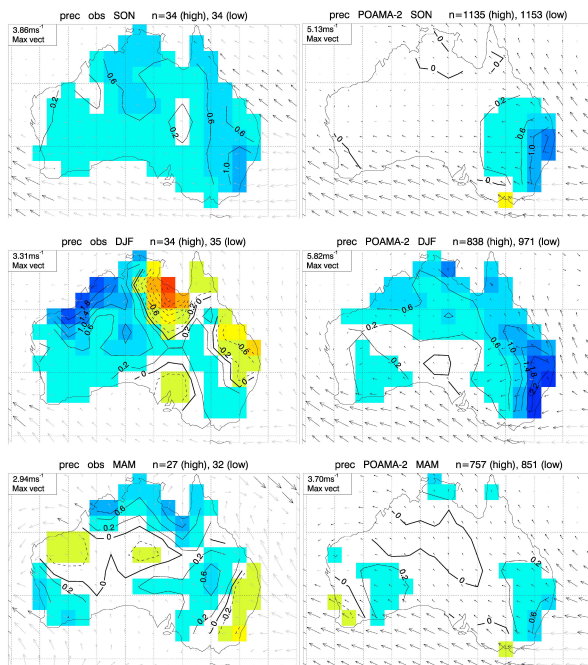
Copyright and Disclaimer

© 2011 CSIRO and the Bureau of Meteorology. To the extent permitted by law, all rights are reserved and no part of this publication covered by copyright may be reproduced or copied in any form or by any means except with the written permission of CSIRO and the Bureau of Meteorology.

CSIRO and the Bureau of Meteorology advise that the information contained in this publication comprises general statements based on scientific research. The reader is advised and needs to be aware that such information may be incomplete or unable to be used in any specific situation. No reliance or actions must therefore be made on that information without seeking prior expert professional, scientific and technical advice. To the extent permitted by law, CSIRO and the Bureau of Meteorology (including each of its employees and consultants) excludes all liability to any person for any consequences, including but not limited to all losses, damages, costs, expenses and any other compensation, arising directly or indirectly from using this publication (in part or in whole) and any information or material contained in it.

Contents

Towards coupled data assimilation: coupled covariance structures	Patricia Okely, Oscar Alves, Debra Hudson and Yonghong Yin	4
Evaluating key drivers of Australian intra-seasonal climate variability in POAMA-2: a progress report	Andrew G. Marshall, Debra Hudson, Matthew C. Wheeler, Harry H. Hendon and Oscar Alves	10
Extensions to the T2 Tsunami Scenario Database	M. Arthur Simanjuntak, Diana Greenslade and Stewart C.R. Allen	17
Evaluation of simulated Australian climate for the Hadley Centre's CAPTIVATE Project	Ian G. Watterson, Anthony C. Hirst and Arnold Sullivan	22



Editors: P.A. Sandery, T. Leeuwenburg, G. Wang, A.J. Hollis, K.A. Day
Enquiries: Dr Paul Sandery p.sandery@bom.gov.au
 CAWCR Research Letters
 The Centre for Australian Weather and Climate Research
 Bureau of Meteorology
 GPO Box 1298 Melbourne VICTORIA 3001

CAWCR Research Letters is an internal serial online publication aimed at communication of research carried out by CAWCR staff and their colleagues. It follows on from its predecessor *BMRC Research Letters*. Articles in *CAWCR Research Letters* are peer reviewed. For more information visit the CAWCR website.

Towards coupled data assimilation: coupled covariance structures

Patricia Okely, Oscar Alves, Debra Hudson and Yonghong Yin

Centre for Australian Weather and Climate Research

Bureau of Meteorology, Melbourne VIC 3001

P.Okely@bom.gov.au

Introduction

The Predictive Ocean Atmosphere Model for Australia (POAMA) is the dynamical seasonal forecast system at the Australian Bureau of Meteorology. POAMA consists of a global coupled ocean-atmosphere model, data assimilation schemes for ocean, land and atmosphere, and an ensemble forecast system (Alves et al. 2003). Like many current systems, data is assimilated separately into the ocean and atmosphere components of the coupled model, to provide initial conditions for the coupled model forecast. There is concern in the intra-seasonal/seasonal prediction community regarding the impact of the imbalance in ocean and atmosphere initial states generated by separate assimilation schemes (Balmaseda and Anderson, 2009). Initialisation shock caused by this imbalance can manifest as spurious features or impede ocean-atmosphere feedbacks, such as those associated with El Niño-Southern Oscillation (ENSO) and Madden-Julian Oscillation (MJO), and thus ultimately degrade the forecast.

We aim to develop a coupled data assimilation system for POAMA, to provide dynamically balanced ocean-atmosphere initial states for the coupled model forecasts. The new scheme would include an extension of the highly successful ocean data assimilation scheme POAMA currently employs. A keystone of this assimilation scheme is the set of background covariances developed from a non-stationary ensemble of ocean states. The new approach would use coupled ocean-atmosphere background covariances derived from an ensemble of the coupled states. The first step was

to examine the coupled covariances obtained from an ensemble set produced by the POAMA coupled model. Here we investigate whether the coupled covariance structures contain realistic information that could be used to enhance the initialisation of important coupled processes.

POAMA Initialisation Schemes

The POAMA coupled model forecasts are currently initialised using an ensemble of ocean, land and atmosphere states generated by separate ocean and atmosphere-land data assimilation schemes. The Atmosphere Land Initialisation scheme (ALI; Hudson et al., 2011) involves running an offline version of the atmospheric model component of POAMA, forced with observed sea-surface temperature (SST, Reynolds et al., 2002), and nudged towards reanalyses from ERA-40 for the period 1960 to Aug 2002 (Uppala et al., 2005) and BoM's operational global NWP system thereafter. Using this method, ALI introduces realistic atmosphere and land initial conditions into the POAMA forecasts and captures the observed intra-seasonal atmospheric state.

The POAMA Ensemble Ocean Data Assimilation Scheme (PEODAS; Yin et al., 2011) involves running an offline version of the oceanic model component of POAMA forced with surface fluxes from atmospheric reanalyses and strong surface relaxation to observed SST, and assimilating sub-surface temperature and salinity data using an approximate form of the ensemble Kalman filter system (EnKF). PEODAS is based on the multi-variate ensemble optimum interpolation system of Oke et al (2005, 2008), but uses covariances from a time evolving model

ensemble. PEOODAS consists of a central run and 11 perturbed ensemble members, generated by small perturbations to the surface forcing. Background error covariances are estimated from an augmented ensemble set (present 11 ensemble perturbations plus perturbations from 9 previous assimilation cycles, spanning 1 month) and used to assimilate observations into the central run. Using this approach has significant computational savings over a traditional EnKF and other complex schemes. By using state-dependent, multi-variate background error covariances from the ocean ensemble, PEOODAS has been able to successfully utilise salinity observations as well as ocean temperature (Wedd et al., In Prep.) and create good initial conditions for the ocean component of the coupled forecast system (Zhao et al., In Prep.).

Note that PEOODAS actually provides an ensemble of ocean initial conditions that can be used to initialise the ensemble members of the POAMA coupled model forecasts. Prior to the development of PEOODAS, POAMA ensemble members were perturbed using lagged ALI atmospheric states as initial conditions. Ideally, atmospheric and oceanic data would be assimilated together into a coupled ensemble, to generate dynamically balanced ocean-atmosphere initial states, ready to use for coupled model forecasts. Therefore we are considering implementing a coupled data assimilation system for POAMA, comprised of a coupled model ensemble and an extension of the PEOODAS scheme to include atmospheric variables. The coupled scheme would use ocean-atmosphere coupled covariances for data assimilation, thus our first step has been to investigate ocean-atmosphere covariances derived from a POAMA coupled model ensemble.

Coupled Model Ensemble

Shi et al. (2009) used the POAMA coupled model to produce a large ensemble of forecasts to study the 1997 El Niño event. The coupled model used in that study was comprised of the BoM unified atmospheric model version 3.0 (BAM 3.0d; Colman et al., 2005) and the Australian Community Ocean Model version 2 (ACOM2; Schiller et al., 2002). BAM 3.0d has a horizontal spectral resolution of T47 and 17 vertical levels. ACOM2 has a zonal grid spacing of 2°, meridional grid spacing of 0.5° within 8° of the

equator and increasing to 1.5° near the poles, and 25 vertical levels (12 in top 185m). The atmosphere and ocean models are coupled using the Ocean Atmosphere Sea Ice Soil (OASIS) coupling software (Valcke et al., 2000), and no flux correction is applied to the exchanged fluxes. See Alves et al. (2003), Hendon et al. (2009), Zhao and Hendon (2009), Rashid et al. (2011) and others for more information about POAMA model details, applications and skill.

Shi et al. (2009) added small random SST perturbations (0.001°C) to the ocean initial state to create a 90-member ensemble with the coupled model, which was run for 9 months from 1 Dec 1996. The ensemble of forecasts all developed an MJO during the first 4 months and warm El Niño-like conditions. We examined the forecast results at different lead times to determine whether the coupled covariance fields from the ensemble captured the ocean-atmosphere interactions associated with MJO and/or ENSO activity and could be used to guide coupled data assimilation.

Coupled Covariances

Coupled covariances were calculated at specific times into the ensemble coupled model forecasts (e.g. 2 months lead). The forecast results at a given lead time had the ensemble mean removed, and then the ensemble perturbations of a reference variable (e.g. SST) at one location (e.g. ocean surface at intersection of dateline and equator) were compared to ensemble perturbations in that variable, and other ocean and atmosphere variables, all across the model domain. The covariances were normalised, following Alves and Robert (2005), then scaled as shown here:

$$cov_{norm} = \frac{\overline{T(x_0)U(x)}}{\text{var}\{T(x_0)\}}$$

$$cov_{incr} = cov_{norm} * \sqrt{\text{var}\{T(x_0)\}}$$

where ‘ cov_{norm} ’ and ‘ cov_{incr} ’ are the normalised and scaled covariances, respectively, for reference variable ‘ T ’ at location ‘ x_0 ’ compared with variable ‘ U ’ at all locations ‘ x ’, ‘ var ’ is variance, and the overbar represents the average over the ensemble. The normalisation provides the covariance in units of U per unit of T . Scaled covariance shows the change in U based on the standard deviation of the reference variable in the

ensemble; a rough guide to how the information from the ensemble covariances would be used

during data assimilation and to allow the covariances to be assessed in units of relevance.

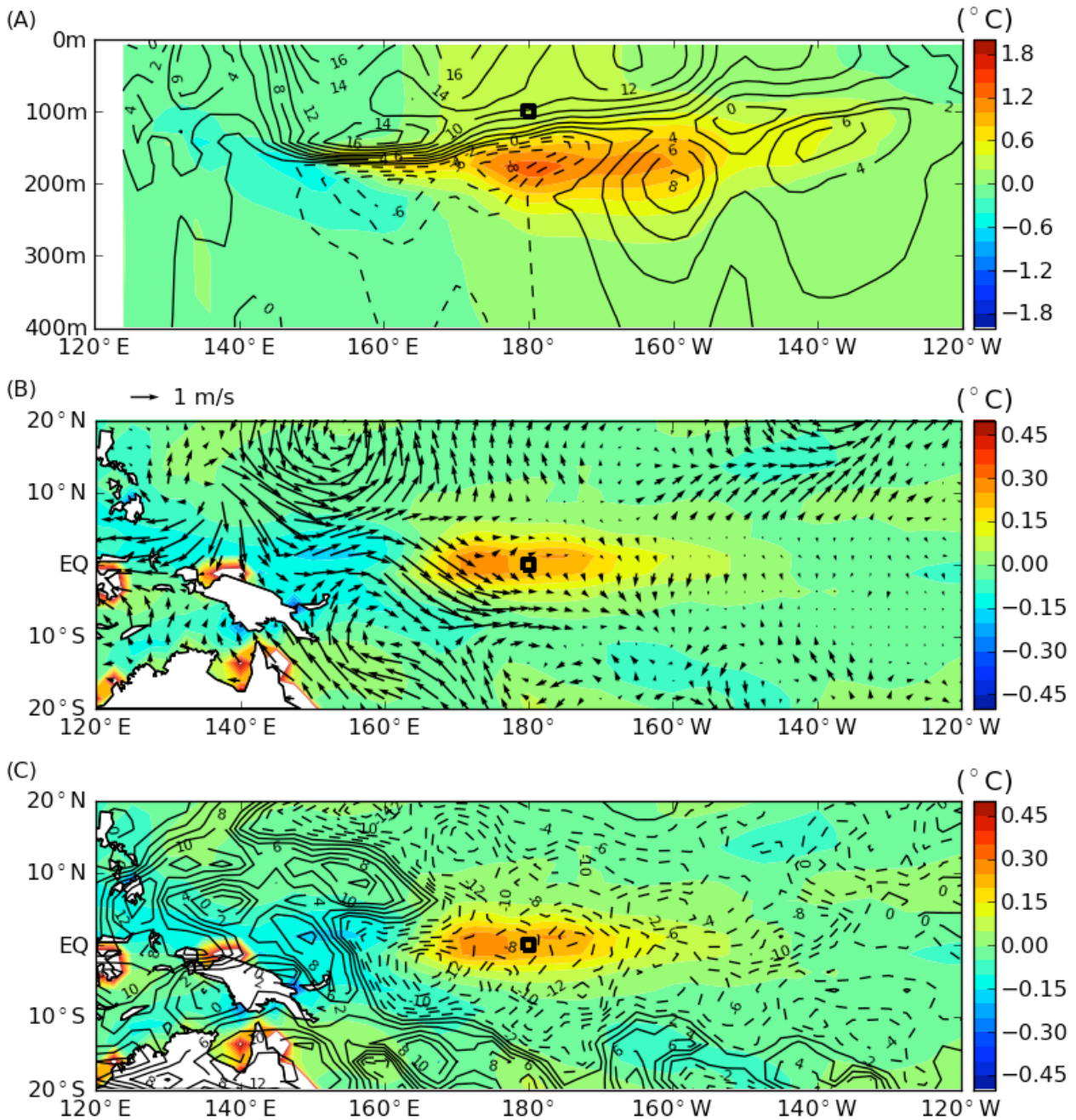


Figure 1 Scaled covariances based on ocean temperature at 100-m depth at (0°, 180°) for ocean temperature (A; shading; °C), ocean zonal current (A; contours; cm s⁻¹), SST (B and C; shading; °C), surface wind (B; vectors; m s⁻¹), and OLR (C; contours; W m⁻²), at 2 months into the coupled model forecasts.

We calculated the coupled covariances in the ensemble after 2 months lead. Around this time the active phase of a strong MJO was centred in the western equatorial Pacific Ocean. Figure 1A

shows an ocean vertical section along the equator in this region, and the shading indicates the covariance of ocean temperature at (0°, 180°) and 100 m depth with temperature elsewhere in the

section. The pattern indicates a positive change in temperature at 100 m is linked to a greater positive adjustment in temperature below; the adjacent negative covariance at the thermocline suggests the local behaviour is associated with downwelling and sharpening of the thermocline, with cooling associated with upwelling further west. Covariance of ocean zonal current with the reference temperature (the contour overlay in Figure 1A) shows that the eastward surface current and underlying counter-current is also congruent with a tilting thermocline.

Figure 1B shows the surface above the vertical section in Figure 1A. In Figure 1B, the shading shows the covariance of SST with the sub-surface reference temperature. A positive change in reference temperature is linked to a local increase of SST. The black vectors in the plot show the change in surface winds associated with positive increase in reference temperature. A more westerly airflow into the region of elevated SST corresponds to an increase in reference

temperature.

In Figure 1C, the shading is again the covariance of SST with the reference temperature. Overlaid are contours of covariance of out-going long-wave radiation (OLR) with the reference temperature; this is a proxy for changes in convection associated with positive change in reference temperature. The covariance field indicates a region of increased convection (decreased OLR) where SST is increased around the reference location.

These patterns, including the pair of atmospheric cyclonic cells off the equator and to the west of the reference location, which feed the westerlies into the region of enhanced convection, are typical of the influence of the MJO. This result is encouraging as it shows how the air-sea interactions important to representing the MJO may be captured by coupled covariances and utilised in coupled data assimilation to improve coupled forecasts.

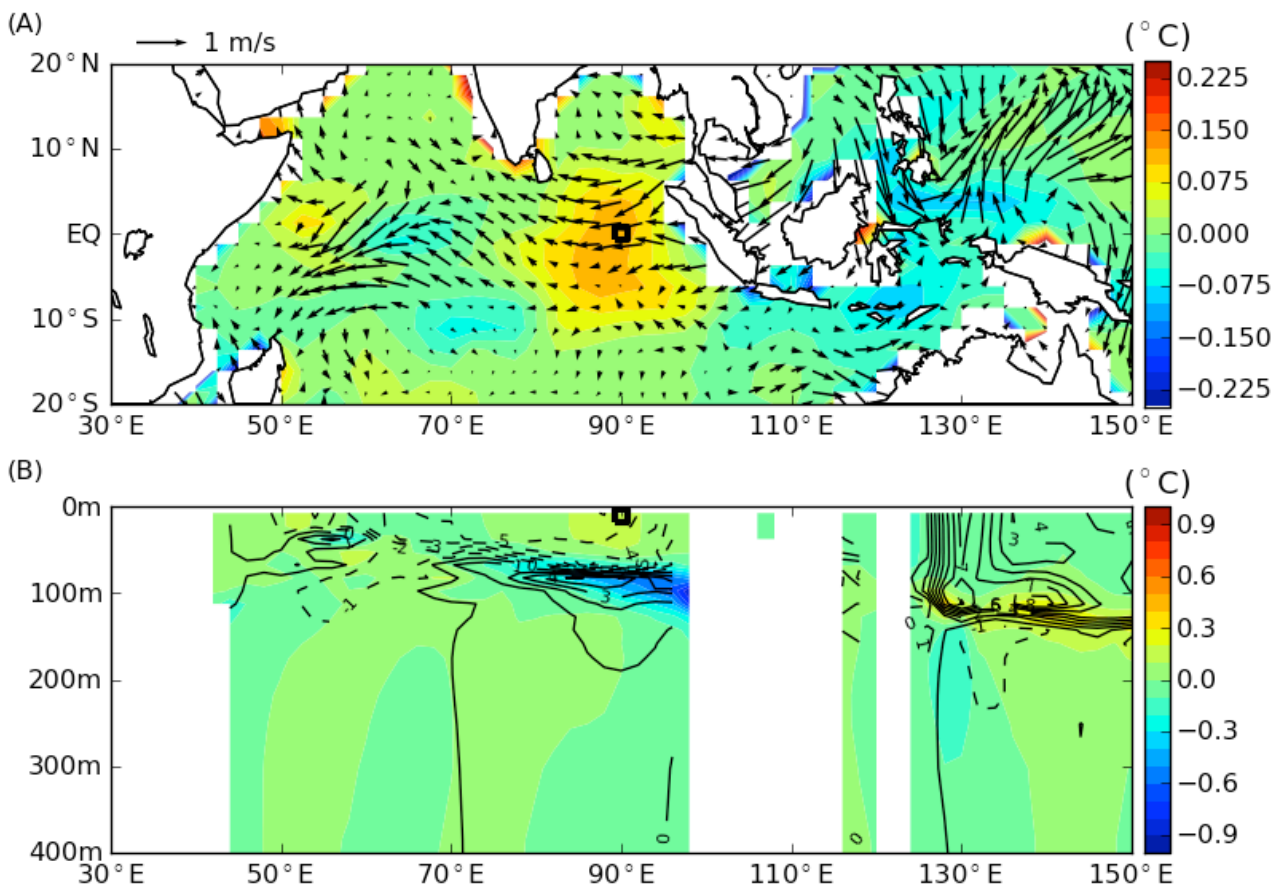


Figure 2 Scaled covariances based on SST at (0°, 90°E) for SST (A; shading; °C), surface winds (A; vectors; $m s^{-1}$), ocean temperature (B; shading; °C), and ocean zonal current (B; contours; $cm s^{-1}$) at 1 month into the coupled model forecasts.

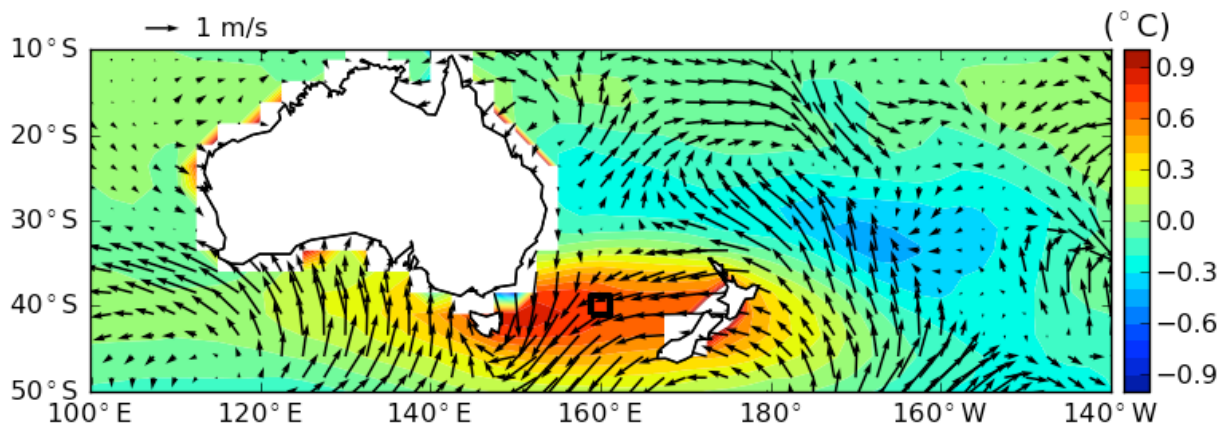


Figure 3 Scaled covariances based on SST at (40°S, 160°E) for SST (shading; °C) and surface winds (vectors; $m s^{-1}$) at 2 months into the coupled model forecasts.

Figure 2 shows covariances with SST in the eastern equatorial Indian Ocean after 1 month of the ensemble forecast. The covariance of SST (Figure 2A, shading), surface winds (Figure 2A, vectors), ocean temperature (Figure 2B, shading) and ocean zonal current (Figure 2B, contours) near the reference point appears to be consistent with enhanced upwelling near the maritime continent. Covariances further afield (for example, the north-east corner of the region shown) may not contain realistic information.

We have also examined coupled covariances in the mid-latitudes. Figure 3 shows covariances for SST off the east coast of Australia two months into the ensemble forecast (shading is SST, vectors are surface winds). These covariance fields likely contain information related to synoptic systems. For example, the influence of high pressure systems on sea surface currents may explain the connection between the sea surface warming and anticyclonic airflow observed in Figure 3.

Further Considerations

In the examples shown above, it is unclear at what distance from the reference location the information contained in the coupled covariances becomes unrealistic and disconnected from the physical processes we have associated with the covariance structures. The ensemble may not be large enough for noise to cancel in the covariances or the covariances may truly be reflecting teleconnections related to the processes occurring near the reference location. PEODAS applies a latitude-dependent localisation to

covariances during data assimilation. The localisation scheme will need further development for coupled covariances as it will need to reflect differences between atmosphere and ocean horizontal and vertical scales.

In the current study, perturbations in the coupled model ensemble were allowed to grow unconstrained by data assimilation cycles. The large spread in the ensemble, especially after 2 months, produced coupled covariance structures associated with dominant modes of intra-seasonal and inter-annual variability. In a coupled data assimilation system with daily assimilation cycles that constrain the spread of the ensemble (and with less ensemble members due to computational practicalities), the coupled covariance structures may be different than shown here.

The Coupled Ensemble Initialisation (CEI) system has recently been developed as another step towards a fully coupled data assimilation system (Yin et al., In Prep.). The first version of the CEI system involves running the POAMA coupled model as an ensemble (as done in PEODAS) and daily nudging the ocean and atmosphere towards reanalyses (as done in ALI). The next step is to include PEODAS in the CEI system, assimilating ocean observations directly into the coupled ensemble. Finally, the PEODAS scheme will be extended to include atmospheric parameters. The analysis produced by the current version of the CEI system will allow us to further investigate coupled covariances in a constrained coupled model ensemble.

Conclusions

Coupled covariances for a range of variables, such as surface winds, SST, out-going long-wave radiation and ocean currents, have been analysed using a large coupled model ensemble. One major finding was the coupled covariance structures for the atmospheric and oceanic equatorial Pacific, based on unfiltered SST and zonal surface wind errors, contained large-scale surface wind circulation patterns, shifts in the ocean thermocline, and regional enhancement or suppression of deep convection and precipitation, which were associated with the MJO and ENSO. The results showed the coupled covariance structures contained realistic information that could enhance the initialisation of these important coupled processes. The results indicate a coupled data assimilation approach using such covariances has potential to improve intra-seasonal/seasonal forecasts.

Acknowledgements

We would like to thank Li Shi for providing the coupled model ensemble data set used during this study. We would like to thank Peter Oke and Robin Wedd for feedback used to improve this manuscript.

References

Alves, O., and C. Robert, 2005. Tropical Pacific Ocean model error covariances from Monte Carlo simulations. *Q J R Meteorol Soc* 131: 3643-3658.

Alves, O., G. Wang, A. Zhong, N. Smith, F. Tzeitkin, G. Warren, A. Schiller, S. Godfrey, and G. Meyers, 2003. POAMA: Bureau of Meteorology operational coupled model forecast system. *Science for Drought: Proceedings of the National Drought Forum, Brisbane, April 2003*, R. Stone and I. Partridge, Eds., Department of Primary Industries, pp. 49-56.

Balmaseda, M., and D. Anderson, 2009. Impact of initialization strategies and observations on seasonal forecast skill. *Geophys Res Lett.* L01701.

Colman, R., L. Deschamps, M. Naughton, L. Rikus, A.

Sulaiman, K. Puri, G. Roff, Z. Sun, G. Embury, 2005. BMRC Atmospheric Model (BAM) version 3.0: comparison with mean climatology. BMRC Research Report No. 108, Bureau of Meteorology, Melbourne.

Hendon, H. H, E. Lim, G. Wang, O. Alves, and D. Hudson, 2009. Prospects for predicting two flavors of El Niño. *Geophys Res Lett.* L19713.

Hudson, D., O. Alves, H. H. Hendon, and G. Wang, 2011. The impact of atmospheric initialisation on seasonal prediction of tropical Pacific SST. *Clim Dyn.* 36: 1155-1171.

Oke, P. R., A. Schiller, D. A. Griffin, and G. B. Brassington, 2005. Ensemble data assimilation for an eddy-resolving ocean model of the Australian region. *Quart. J. Roy. Meteor. Soc.* 131: 3301-3311.

Oke, P. R., G. B. Brassington, D. A. Griffin, and A. Schiller, 2008. The Bluelink ocean data assimilation system (BODAS). *Ocean Modelling* 21: 46-70.

Reynolds, R., Rayner, N. A., T. M. Smith, D. C. Stokes, and W. Wang, 2002. An improved in situ and satellite SST analysis for climate. *J Clim* 15: 1609-1625.

Rashid, H. A, H. H Hendon, M. C Wheeler, and O. Alves, 2011. Prediction of the Madden-Julian oscillation with the POAMA dynamical prediction system. *Clim Dyn.* 36: 649-661.

Schiller, A., J. Godfrey, P. McIntosh, G. Meyers, N. Smith, O. Alves, O. Wang, and R. Fiedler, 2002. A new version of the Australian Community Ocean Model for Seasonal Climate Prediction. CSIRO Marine Research Report No. 240, CSIRO, Australia.

Shi, L., O. Alves, H. H. Hendon, G. Wang, and D. Anderson, 2009. The role of stochastic forcing in ensemble forecasts of the 1997/98 El Niño. *J Clim* 22: 2526-2540.

Uppala, S. M., P. W. Kallberg, A. J. Simmons et al., 2005. The ERA-40 re-analysis. *Q J R Meteorol Soc* 131: 2961-3012.

Valcke, S., L. Terray, and A. Piacentini, 2002. Oasis 2.4, Ocean atmosphere sea ice soil: user's guide. TR/CMGC/00/10, CERFACS, Toulouse, France.

Yin, Y., O. Alves, and P. R. Oke, 2011. An ensemble ocean data assimilation system for seasonal prediction. *Mon Wea Rev.* 139: 786-808.

Zhao, M., and H. H Hendon, 2009. Representation and prediction of the Indian Ocean dipole in the POAMA seasonal forecast model. *Q J R Meteorol Soc* 135: 337-352.

Evaluating key drivers of Australian intra-seasonal climate variability in POAMA-2: a progress report

Andrew G. Marshall^A, Debra Hudson^B, Matthew C. Wheeler^B, Harry H. Hendon^B and Oscar Alves^B

Centre for Australian Weather and Climate Research

^ACastray Esplanade, Hobart, Tasmania, 7000

^B700 Collins Street, Docklands, Victoria, 3008

andrew.marshall@csiro.au

Introduction

The use of the Bureau of Meteorology's dynamical Predictive Ocean Atmosphere Model for Australia (POAMA; Alves et al. 2003) as an intra-seasonal prediction tool for Australia is currently being investigated. POAMA was originally designed for forecasting seasonal mean conditions (e.g. mean conditions for the upcoming three months). However users of climate forecasts, such as in agriculture and water management, are increasingly seeking forecast guidance on time scales and lead times shorter than seasonal. The new version of the model, POAMA-2, has been developed to better suit forecasting at these multi-week timescales, thereby filling the gap in current prediction capability between weather forecasts and seasonal outlooks for Australia. This work is part of the process towards development of dynamical modeling as the basis for Australia's weather and climate forecasts.

One of the main targets of this research is to improve our understanding of climate drivers that control intra-seasonal climate variability and forecast skill in POAMA-2. This paper summarises our progress on evaluating the role of two key drivers: the Madden-Julian Oscillation (MJO) and the Southern Annular Mode (SAM). Specifically, we assess the model's ability to (i) predict the large-scale components of each driver, (ii) simulate the associated rainfall with each driver, and (iii) predict rainfall regionally where each driver has a large impact.

Model description

POAMA-2 uses the Bureau of Meteorology

unified atmospheric model version 3 (Colman et al. 2005) and the Australian Community Ocean Model version 2 (Schiller et al. 1997). Initial conditions are provided by separate data assimilation schemes for the ocean, land and atmosphere components of the global coupled model; for POAMA-2 these include an ensemble ocean data assimilation system (PEODAS; Yin et al. 2011) and an atmosphere/land initialisation system (ALI; Hudson et al. 2011). PEODAS is an approximate form of the ensemble Kalman filter system and generates an ensemble of ocean states each day including a central unperturbed ocean analysis. ALI creates a set of realistic atmospheric initial states by nudging zonal and meridional winds, temperatures and humidity from the atmosphere model of POAMA (run prior to hindcasts being made and forced with observed SST) toward an observationally based analysis. ALI also generates land surface initial conditions that are in balance with the atmospheric condition; see Hudson et al. (2011) for full details of the ALI system.

Perturbed initial conditions, which are required to sample forecast uncertainty due to sensitivity to initial condition errors, are provided using a coupled breeding technique. The coupled breeding produces consistent perturbations to both the ocean and atmosphere at the initial time of the forecasts. The perturbations are generated using the coupled ocean-atmosphere model and then rescaled to represent analysis uncertainty and centred every day, and added to the unperturbed analyses. This new strategy represents a significant milestone in our development of the POAMA forecast system for

intra-seasonal prediction.

Data description

The POAMA-2 hindcast framework consists of a 33-member ensemble of 4 months duration initialized on the 1st, 11th and 21st of each month between 1989 and 2010. Here we use the period 1989–2006 that is common to POAMA-1.5. In contrast to POAMA-1.5, POAMA-2 also uses a multi-model approach whereby three model versions each producing 11 ensemble members are used to create the 33-member ensemble. We analyse the first 8 weeks of precipitation, zonal wind, meridional wind, and diurnal maximum temperature data for hindcasts initialized on the 1st of the month. Hindcast anomalies are formed relative to the hindcast model climatology, which is a function of both start month and lead time, and thus a first-order linear correction for model mean bias is made. We define a lead time of one week as the mean of the first week of each hindcast.

Model generated Australian rainfall and temperature data are verified against Australian National Climate Centre (NCC) 0.25° gridded daily data (Mills et al. 1997) interpolated onto the POAMA spatial grid. Global rainfall simulations and predictions are verified against the Climate Prediction Centre Merged Analysis of Precipitation pentad dataset (CMAP; Xie and Arkin 1997). Model generated global wind data are verified against ERA-40 data (Uppala et al. 2005) for the years 1980–2001. We create anomalies, relative to climatology, from the observational/re-analysis datasets for direct comparison with POAMA-2 anomalies.

Madden-Julian Oscillation

As the dominant mode of tropical intra-seasonal variability, the MJO (e.g. Madden and Julian 1994) exerts an important influence on weather and climate in many parts of the globe including Australia (Wheeler et al. 2009). The MJO consists of large-scale coupled patterns in atmospheric circulation and deep convection that propagate eastward over the equatorial Indian and western Pacific oceans with a period of 30–90 days. The state of the MJO is depicted using the bivariate Real-time Multivariate MJO (RMM) index, which captures the large-scale structure of the MJO in zonal wind and convection along the equator; see Wheeler and Hendon (2004) for full

details. The RMM index is obtained from a combined EOF analysis of equatorially-averaged (15°N–15°S) outgoing longwave radiation (OLR), 850hPa zonal wind, and 200hPa zonal wind anomalies using NCEP/NCAR reanalysis data.

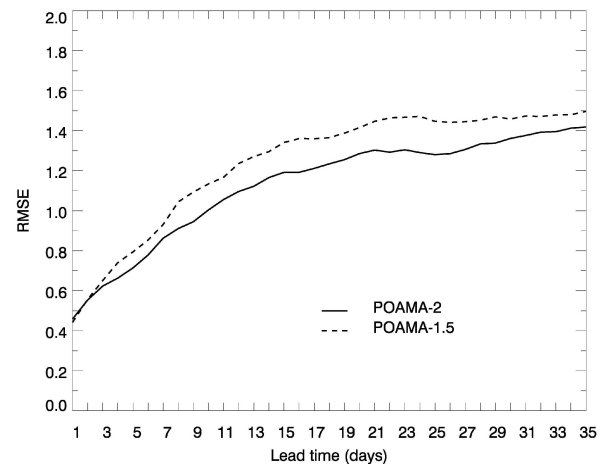


Figure 1 Root-mean-square error of the predicted RMM index for the ensemble mean POAMA-2 (solid) and POAMA-1.5 (dashed) forecast as a function of lead time (days) for all hindcasts initialized 1989–2006.

Figure 1 illustrates the skill in predicting the daily RMM index for POAMA-2 (solid) and POAMA-1.5 (dashed). We score the daily ensemble mean RMM index for each model using root-mean-square error (RMSE), which is calculated as a function of forecast start month over the hindcast period 1989–2006 for lead times out to 30 days. For a climatological forecast of the bivariate RMM anomaly index the $RMSE = \sqrt{2}$, and thus forecasts are typically deemed to be skilful for $RMSE < \sqrt{2}$. However, Figure 1 shows the approach to $\sqrt{2}$ at long lead time is slow, so we can more confidently say that POAMA-2 provides about a 1-week improvement in skill compared to POAMA-1.5 for lead times beyond about 2 weeks.

With our focus on the global-scale impact of the MJO, we assess the ability of POAMA-2 to reproduce the broad-scale spatial structure of MJO rainfall on intra-seasonal timescales. Figure 2 shows composite maps of weekly-mean rainfall based on the 8 phases of the MJO lifecycle defined by Wheeler and Hendon (2004), for observations and POAMA-2. Model composites

are formed using lead times 3–6 weeks so as to be independent of initial conditions and model spin-up, and we combine adjacent MJO phase pairs corresponding to the convectively active phase of the MJO over the Indian Ocean (2/3), Maritime Continent (4/5), western Pacific (6/7), and Western Hemisphere (8/1). We present composite MJO-rainfall anomalies in Figure 2 for November–April when the MJO is strongest and shifted into the Southern Hemisphere.

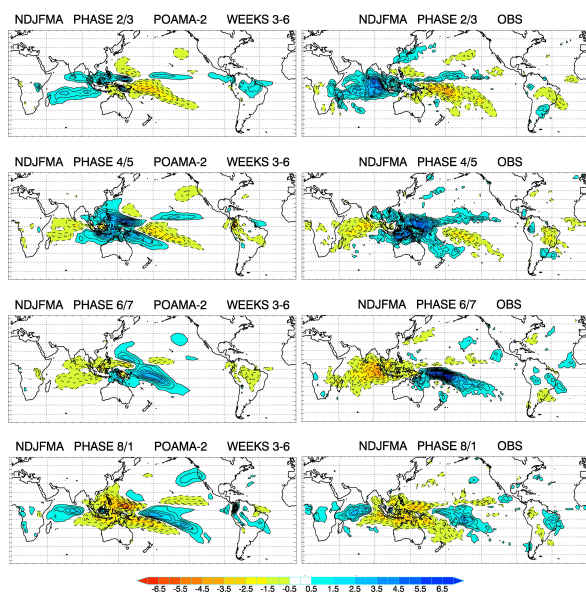


Figure 2 Rainfall anomaly composite maps for MJO phases 2/3, 4/5, 6/7, and 8/1 over the period November–April for POAMA-2 hindcasts at lead times of 3–6 weeks (left column) and for observations (right column).

POAMA-2 reproduces the observed broad-scale characteristics of each MJO phase with reasonable fidelity over the Indian and western Pacific Ocean (Indo-Pacific) region, including over northern Australia. The model also captures some features of the MJO’s impact on tropical rainfall away from the Indo-Pacific region, with anomalous drying (wet conditions) over parts of Brazil and equatorial Africa in phases 4/5 (8/1). A notable deficiency, however, is the underestimation of the magnitude of the rainfall anomaly over the eastern Indian Ocean by up to 50%, which is particularly evident in phases 2/3 and 6/7 when the rainfall anomaly peaks over this region. The POAMA-2 representation of MJO rainfall shown here is similar to that of POAMA-1.5 (Marshall et al. 2010a), which is not surprising given that the atmospheric models in

POAMA-2 and POAMA-1.5 are similar.

Based on the knowledge that (i) POAMA-2 can predict the large-scale structure of the MJO out to 4 weeks (Figure 1) and (ii) the local signal of the MJO in rainfall across the Indo-Pacific is generally well simulated (Figure 2), we turn our attention to the ability of the model to predict rainfall at intra-seasonal timescales in association with the MJO. Probabilistic verification for the second fortnight (comprising the average of forecast weeks 3 and 4) for November–April start times is shown in Figure 3 using the Relative Operating Characteristic (ROC) for rainfall in the upper tercile for forecasts with and without an MJO event in the initial conditions. There are 73 cases where the MJO is strong at the initial time (RMM index ≥ 1 standard deviation, in any phase) and 35 cases where it is weak (RMM index < 1). The ROC score measures the ability of the forecasting system to discriminate between events and non-events, thereby providing information on forecast resolution. In Figure 3 we use pink shading for ROC scores greater than 0.6, with scores greater than 0.5 indicating forecast skill better than climatology.

The high ROC scores across the equatorial Pacific for both strong and weak MJO cases (Figure 3) owe their existence to the high predictability of rainfall associated with the El Niño–Southern Oscillation (ENSO), which is largely independent of the presence or absence of the MJO in the initial condition. Elsewhere, POAMA-2 shows a larger and more cohesive spatial coverage of ROC scores greater than 0.6 over parts of the Indo-Pacific (extending into the North Pacific), North Atlantic Ocean, and eastern Australia when the MJO is strong at the initial time, compared with when the MJO is weak at the initial time. The MJO is known to have a strong direct impact over the Indo-Pacific, and thus we expect the MJO to be important for intra-seasonal prediction over this region. Atmospheric teleconnections of the MJO are known to modulate local climate over eastern Australia (Wheeler et al. 2009) and the North Atlantic Ocean (e.g. Cassou 2008), and thus the MJO also appears to be a source of intra-seasonal rainfall predictability over these extra-tropical regions; this is a key result in the development of POAMA-2 for intra-seasonal prediction. We further note that the ROC skill for predicting

MJO-rainfall over these tropical and extra-tropical regions is considerably higher and more spatially cohesive for POAMA-2 than for POAMA-1.5 (not shown) in the second fortnight, consistent with the vast improvement in predicting the MJO index in POAMA-2 (out to 4 weeks) compared with POAMA-1.5 (3 weeks; Figure 1).

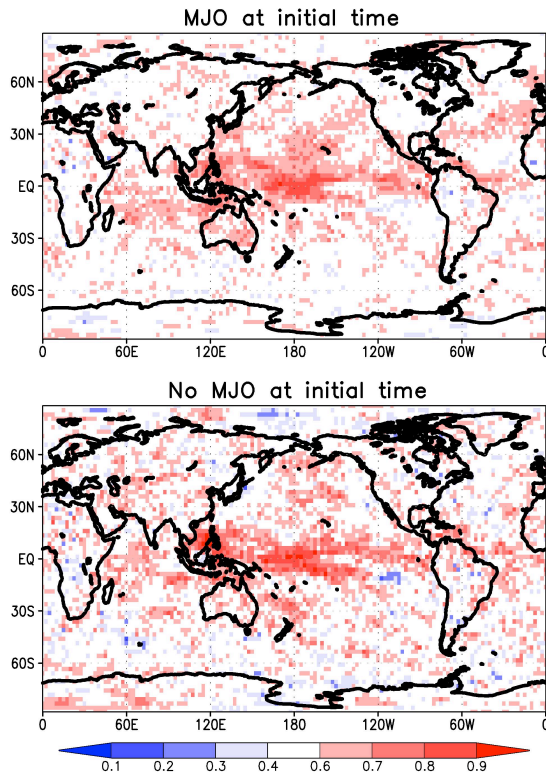


Figure 3 ROC scores of the probability that precipitation averaged over days 15-28 is in the upper tercile for Nov-Apr forecast start months for cases with an MJO in the initial conditions (top) and with no MJO in the initial conditions (bottom).

Southern Annular Mode

The SAM (e.g. Trenberth 1979) plays a dominant role in the high- and mid-latitude climate of the Southern Hemisphere. Characterised by meridional shifts in the strength of the zonal flow between about 55°-60°S and 35°-40°S, the high polarity index of the SAM is described by decreased geopotential height over the polar cap, increased geopotential height over the mid-latitudes, and a poleward shift of the mid-latitude westerly wind belt over the Southern Ocean. SAM variations are consistent with a normally distributed red-noise process with an e-folding timescale of around 10 days, with variability in the SAM found over a wide range of timescales.

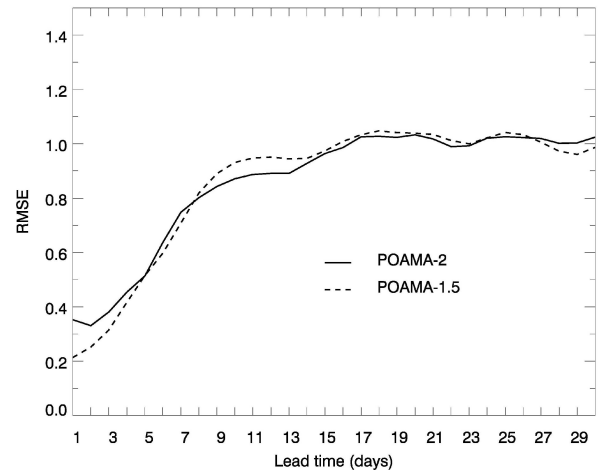


Figure 4 As for Figure 1 except for the SAM index.

The SAM is represented by an index that captures the variability of MSLP around the mid-latitudes of the Southern Hemisphere (e.g. Gong and Wang 1999). The observed and model SAM indices are obtained from an EOF analysis of zonal-mean MSLP between 25°S and 75°S, using NCEP/NCAR Re-analysis data and POAMA hindcast data respectively; see Marshall et al. (2011b) for full details. Figure 4 illustrates the skill in predicting the ensemble mean daily SAM index for POAMA-2 (solid) and POAMA-1.5 (dashed). For a climatological forecast of the SAM index the RMSE=1; POAMA-2 reaches this threshold after 16 days, compared with 15 days for POAMA-1.5. Thus, the new model is a slight improvement on its predecessor in its ability to predict the SAM. The inherent strong persistence of the SAM appears to be a key factor for its extended-range predictability in a dynamical forecast model (Marshall et al. 2011b).

We assess the ability of POAMA-2 to reproduce observed relationships between the SAM and intra-seasonal regional rainfall anomalies in the Australian region. We define the high index polarity (positive phase) and low index polarity (negative phase) of the SAM as occurring when index values exceed one standard deviation (σ) about the mean (i.e. $> 1\sigma$ and $< -1\sigma$ respectively). To first order, the high and low index polarities have opposite signed but otherwise identical climate impacts, and thus we calculate the high-minus-low index composite difference to describe anomalous conditions during the positive phase of the SAM.

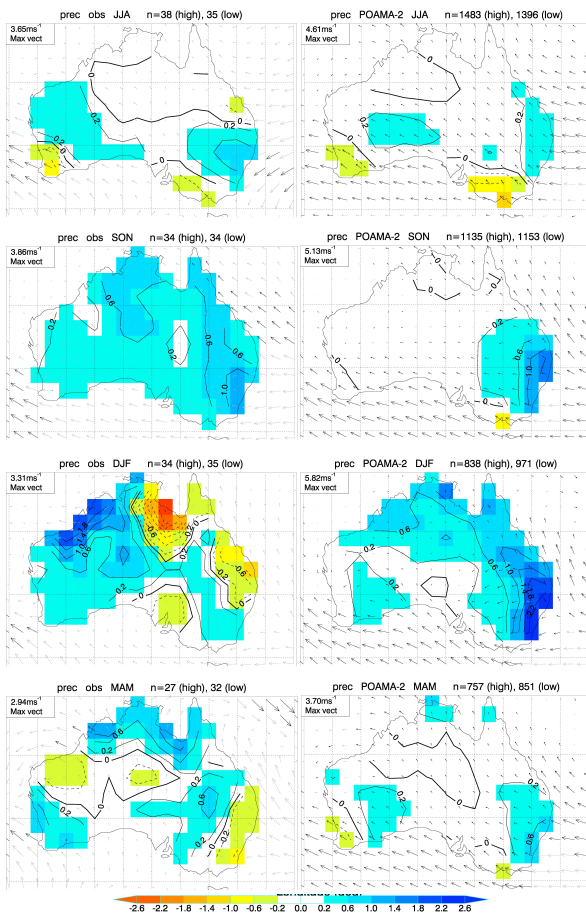


Figure 5 Weekly-mean composites of rainfall and 10m wind vectors for the high-minus-low index polarity of the SAM in JJA (top row), SON (second row), DJF (third row), and MAM (bottom row), for observations (left column) and POAMA-2 hindcasts averaged over lead times of 3-6 weeks (right column). The total number of cases for the high and low SAM polarities is shown in the title

Figure 5 shows composite maps of weekly-mean rainfall in association with the positive phase of the SAM from the observed and model data for lead times 3-6 weeks. We note that the southernmost island state of Tasmania is not resolved as landmass in POAMA due to characteristics of the model grid and resolution, and thus we only consider the mainland of Australia here. POAMA-2 best reproduces the observed SAM-rainfall relationship in the JJA and SON seasons. In particular for JJA, the model captures the decrease in rainfall over the tip of SWWA and over south-eastern Australia to the west of the Australian Alps as reported by Hendon et al. (2007). Reasonable agreement between modeled and observed SAM-rainfall is

also achieved over some parts of Australia in DJF and MAM, although the impact of the SAM on increased rainfall in DJF is stronger than observed over the southeast and weaker than observed over the northwest. And, over parts of northern Australia in DJF, the positive rainfall anomalies in the model appear in contrast to the negative anomalies observed. We note that the POAMA-2 representation of SAM rainfall in all seasons is very similar to that of POAMA-1.5 shown in Marshall et al. (2011b).

In general for all seasons, the larger-than-observed rainfall increases during high SAM over eastern Australia can be explained by the fact that POAMA shows a bias in its representation of the SAM, as demonstrated by composite maps of MSLP (shown in Marshall et al. 2011b for POAMA-1.5 with a similar representation for POAMA-2; not shown). Although POAMA simulates the large-scale characteristics of the SAM reasonably well, a positive MSLP bias develops to the south of Australia over the first few weeks of the hindcast which highlights the impact of model errors and a drifting basic state on the depiction of the SAM as the model atmosphere spins up to reach its preferred climatology. This positive MSLP bias leads to an intensification of the south-easterly anomalies around the southern and eastern perimeters of Australia, relative to those observed (seen in all seasons in Figure 5), which act to drive more moisture from the surrounding oceans to the southern and eastern fringes of the continent and thus impact the representation of SAM-rainfall in the model.

Based on the knowledge that (i) POAMA-2 provides skilful prediction of the SAM index beyond 2 weeks (Figure 4), and (ii) that the teleconnection between the SAM and extratropical rainfall over Australia is best simulated in JJA and SON (Figure 5), we turn our attention to the ability of the model to predict winter/spring rainfall for weeks 2 and 3 in association with the SAM. Verification for the fortnight comprising the average of weeks 2 and 3 in June-November (JJASON) forecast start months is shown in Figure 6 in the form of correlation, which measures the linear correspondence between the ensemble mean forecast and observed. We further stratify the

data according to the strength of the SAM index at the initial time by defining “large SAM” (38 cases) as occurring when the index is either high (greater than the mean plus 1 standard deviation) or low (less than the mean minus 1 standard deviation), and “small SAM” (39 cases) as occurring when the absolute magnitude of the SAM index is less than the mean plus half a standard deviation. We remove the impact of ENSO by omitting El Niño and La Niña years from the analysis, since ENSO negatively correlates to SAM in spring.



Figure 6 Correlation skill for forecasting rainfall (top) and maximum temperature (bottom) in JJASON during the fortnight comprising the average of weeks 2 and 3 when the magnitude of the SAM is large (left) and small (right) at the initial time. Statistically significant correlations are shaded (95% confidence level; t-test).

Figure 6 clearly shows significantly higher skill in forecasting rainfall in weeks 2 and 3 during JJASON over much of south-eastern Australia when the SAM is large compared to when it is small. Having identified south-eastern Australia as being affected by the SAM on intra-seasonal timescales both in observations and in the model in JJA and SON (Figure 5), our results show that the SAM contributes to intra-seasonal rainfall predictability. A similar result is seen for forecasting maximum temperature, with POAMA-2 in fact producing higher correlation skill over most of the continent when the SAM is large compared to when it is small (Figure 6).

We further note that the skill for predicting SAM-related anomalies in POAMA-2 shows a small improvement upon POAMA-1.5 (not shown) for rainfall over the southwest and

northeast, and for maximum temperature over most of continent, consistent with the slight improvement in skill for predicting the SAM index in POAMA-2 compared with POAMA-1.5 (Figure 4).

Conclusions

The new POAMA-2 intra-seasonal forecast system demonstrates improved skill compared to POAMA-1.5 in predicting the MJO and SAM, as embodied by the increased ability to predict the RMM index by about 1 week lead time and the SAM index by about 1 day lead time. The spatial structure of simulated rainfall in association with each climate driver in weeks 3-6 is comparable to that in POAMA-1.5, however the improved prediction of the MJO and SAM indices in POAMA-2 translates into improvements in intra-seasonal prediction of Australian rainfall anomalies in association with the MJO in November-April and the SAM in June-November. We attribute these increases in skill to the production of perturbed initial conditions using coupled breeding that were introduced in POAMA-2.

Analysis of forecast skill in the three individual model versions of POAMA-2 give similar results (not shown), suggesting that there is little benefit to the present multi-model approach at intra-seasonal timescales. This is because each model version uses the same set of perturbed initial conditions, and as such the benefit of using different model formulations is only evident at much longer lead times for which ensemble spread develops as a result of model differences (Wang et al. 2011). Future development of POAMA will include using different perturbed initial conditions for each model version, to better simulate ensemble spread at intra-seasonal timescales.

Real-time forecasts using POAMA-2 are now being produced as experimental products on the POAMA web site for feedback from applications research groups. This feedback is assisting with the operational development of POAMA for seamless prediction across synoptic, intra-seasonal and seasonal timescales.

Acknowledgements

Support for this work was provided by the Managing Climate Variability Program of Grains

Research and Development Corporation, and the Western Australian Marine Science Institution.

References

- Alves, O., G. Wang, A. Zhong, N. Smith, F. Tzeitkin, G. Warren, A. Schiller, S. Godfrey and G. Meyers, 2003: POAMA: Bureau of Meteorology Operational Coupled Model Forecast System. In: Proceedings of national drought forum, Brisbane, April 2003, pp 49-56. Available from DPI Publications, Department of Primary Industries, GPO Box 46, Brisbane, Qld 4001, Australia.
- Cassou, C., 2008: Intraseasonal interaction between the Madden-Julian Oscillation and the North Atlantic Oscillation. *Nature*, **455**, 523-527.
- Colman, R., L. Deschamps, M. Naughton, L. Rikus, A. Sulaiman, K. Puri, G. Roff, Z. Sun and G. Embury, 2005: BMRC Atmospheric Model (BAM) version3.0: comparison with mean climatology. BMRC Research Report no. 108, Bur. Met., Melbourne, Australia.
- Gong, D. and S. Wang, 1999: Definition of Antarctic Oscillation index. *Geophys. Res. Lett.*, **26**, 459-462.
- Hendon, H.H., D.W.J. Thompson and M.C. Wheeler, 2007: Australian Rainfall and Surface Temperature Variations Associated with the Southern Hemisphere Annular Mode. *J. Clim.*, **20**, 2452-2467.
- Hudson, D., O. Alves, H.H. Hendon and G. Wang, 2011: The impact of atmospheric initialisation on seasonal prediction of tropical Pacific SST. *Clim. Dyn.*, **36**, 1155-1171.
- Madden, R.A. and P.R. Julian, 1994: Observations of the 40–50 day tropical Oscillation - a review. *Mon. Wea. Rev.*, **122**, 814-837.
- Marshall, A.G., D. Hudson, M.C. Wheeler, H.H. Hendon and O. Alves, 2011a: Assessing the simulation and prediction of rainfall associated with the MJO in the POAMA seasonal forecast system. *Clim. Dyn.*, **37**, 2129-2141.
- Marshall, A.G., D. Hudson, M.C. Wheeler, H.H. Hendon and O. Alves, 2011b: Simulation and prediction of the Southern Annular Mode and its influence on Australian intra-seasonal climate in POAMA. *Clim. Dyn.*, doi:10.1007/s00382-011-1140-z.
- Mills, G.A., G. Weymouth, D.A. Jones, E.E. Ebert and M.J. Manton, 1997: 'A national objective daily rainfall analysis system' BMRC Techniques Development Report No.1, Bureau of Meteorology, Australia.
- Schiller, A., J.S. Godfrey, P. McIntosh and G. Meyers, 1997: A global ocean general circulation model climate variability studies. CSIRO Marine Research Report No. 227.
- Smith, N.R., J.E. Blomley and G. Meyers, 1991: A univariate statistical interpolation scheme for subsurface thermal analyses in the tropical oceans. *Prog. Oceanogr.*, **28**, 219-256.
- Trenberth, K.E., 1979: Interannual variability of the 500 mb zonal-mean flow in the Southern Hemisphere. *Mon. Wea. Rev.*, **107**, 1515-1524.
- Uppala, S.M., P.W. Kallberg, A.J. Simmons, U. Andrae, V. Da Costa Bechtold, M. Fiorino, J.K. Gibson, J. Haseler, A. Hernandez and G.A. Kelly, 2005: The ERA-40 re-analysis. *Q. J. R. Meteorol. Soc.*, **131**, 2961-3012.
- Wang G., D. Hudson, Y. Yin, O. Alves, H. Hendon, S. Langford, G. Liu, and F. Tseitkin, 2011. POAMA-2 SST Skill Assessment and Beyond. *CAWCR Research Letters*, **6**, 40-46.
- Wheeler, M.C. and H.H. Hendon, 2004: An all-season real-time multivariate MJO index: Development of an index for monitoring and prediction. *Mon. Wea. Rev.*, **132**, 1917-1932.
- Wheeler, M.C., H.H. Hendon, S. Cleland, H. Meinke and A. Donald, 2009: Impacts of the Madden-Julian Oscillation on Australian Rainfall and Circulation. *J. Clim.*, **22**, 1482-1498.
- Xie, P. and P.A. Arkin, 1997: Global precipitation: A 17-year monthly analysis based on gauge observations, satellite estimates, and numerical model outputs. *Bull. Am. Meteorol. Soc.*, **78**, 2539-2558.
- Yin, Y., O. Alves and P.R. Oke, 2011: An ensemble ocean data assimilation system for seasonal prediction. *Mon. Wea. Rev.*, **139**, 786-808.

Extensions to the T2 Tsunami Scenario Database

M. Arthur Simanjuntak, Diana J.M. Greenslade, Stewart C.R. Allen

Centre for Australian Weather and Climate Research

700 Collins Street, Docklands, Victoria, 3008

a.simanjuntak@bom.gov.au

Introduction

A second-generation tsunami scenario database, named T2, has been developed to provide guidance for the Joint Australian Tsunami Warning Centre (JATWC), and is documented in Greenslade *et al.* (2009). As of 2010, the T2 scenario database consisted of 1,865 scenarios representing tsunamis generated by earthquakes of magnitudes of $M_w = 7.5$, 8.0, 8.5 and 9.0. With linear scaling, the T2 scenarios can provide guidance for earthquake magnitudes ranging from $M_w = 7.3$ to $M_w = 9.2$. Analysis of the water elevation from the T2 scenarios in the Australian coastal zones suggests that an earthquake of magnitude below $M_w = 7.0$ would not generate any warnings for Australia (Greenslade *et al.* 2009), however there is a need to provide forecast

guidance for tsunamis generated by earthquakes of smaller magnitudes due to JATWC's commitment to operate as a Regional Tsunami Service Provider within the Indian Ocean Tsunami Warning System (JATWC, 2011). This paper describes a series of additional magnitude 7.0 scenarios, as well as a further individual scenario which have been added to the T2 scenario database.

Magnitude 7.0 scenarios

The earthquake parameters for the existing scenarios are shown in the yellow shaded areas in Table 1 (reproduced from Greenslade *et al.* 2009). The new scenarios described in this paper are shaded in blue.

Table 1 Rupture dimensions for T2 scenario database

Number of scenarios	Magnitude M_w	Seismic moment M_o (Nm)	Width W (km)	Number of rupture elements	Length (approx.) L (km)	Slip u_o (m)
203	7.0	3.9×10^{19}	35	1	50	0.5
521	7.5	2.24×10^{20}	50	1	100	1
521	8.0	1.26×10^{21}	65	2	200	2.2
471	8.5	7.2×10^{21}	80	4	400	5
351	9.0 (standard)	4.0×10^{22}	100	10	1000	8.8
1	9.0 (Sandwich only)	4.0×10^{22}	100	8	800	11
1	9.0 (Puysegur only)	4.0×10^{22}	100	6	600	14.7

The choice of the dimensions and locations of the $M_w = 7.0$ scenarios is not straightforward and this section discusses the approach taken. The specific characteristics of the ruptures that must be predetermined are the rupture length, width, slip and epicentre location. However, there is limited data on the typical range of rupture dimensions for subductive type $M_w = 7.0$

earthquakes. A reliable estimate of rupture length (L) can be extracted from the slip-predictable model of past subductive earthquakes of Pacheco *et al.* (1993) (heretofore referred to as Pac93). In Figure 1, the compiled L - M_w relationship from the data in Table 4 of Pac93 is shown. The moment magnitude in this Figure was derived from seismic moment (M_o)

following Hanks and Kanamori (1979):

$$M_w = \frac{2}{3}(\log_{10} M_o - 9.1)$$

Since the relationship shown in Figure 1 is scattered, and there are only three points for $6.8 < M_w < 7.0$, a correlation analysis is not feasible. However, inspection suggests that a length of 50 km $< L < 70$ km is a reasonable range.

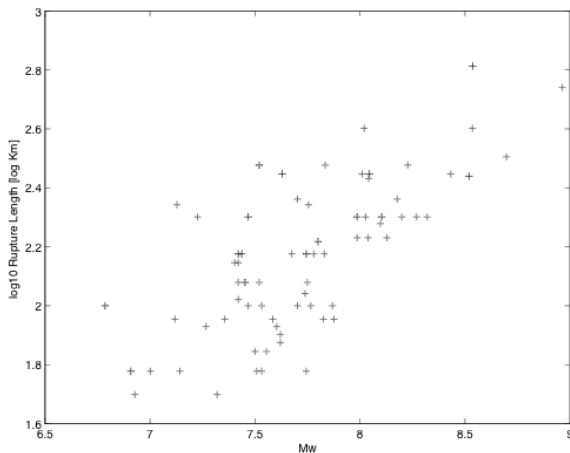


Figure 1 Rupture length against magnitude for subductive earthquakes, compiled from the data presented in Pacheco et al. (1993).

Pac93 showed that estimates of rupture width (W) from smaller earthquakes are unreliable due to limited and highly scattered data, although inspection of Figure 13e in Pac93 suggests that a value of 50km is a reasonable value for width.

Wells and Coppersmith (1994) (heretofore referred to as WC94) derived correlations between rupture dimensions and M_w from extensive earthquake data, but subductive earthquakes were excluded. However it is worth noting that for all the types of earthquakes presented, their correlations for $M_w = 7.0$ earthquakes yield 30 km $< L < 50$ km and 13 km $< W < 20$ km. In addition, they present a very tight correlation between rupture area (A) and M_w , yielding $A \sim 1000$ km² for $M_w = 7.0$ earthquakes. These values are somewhat consistent with Pac93. Note that in order to derive the values above, we used the equations presented in Table 2A in WC94, incorporating the standard deviations in order to obtain the maximum range of values.

WC94 observed included a more scattered slip relationship. For $M_w = 7.0$, these correlations yield slip values of 0.5m $< u_o < 2.5$ m for ruptures with length values of 40 km $< L < 70$ km.

Summary of Possible Rupture Dimensions

Based on the discussion above, it appears that realistic rupture dimensions for $M_w = 7.0$ earthquakes are:

Length (L):	30 – 70 km
Width (W):	13 – 50 km
Slip (u_o):	0.5 - 2.5 m

In order to maintain continuity within the T2 scenario database, the choice of width should ideally be less than the $M_w = 7.5$ widths of 50 km. On the other hand, the lower limit for width above, although physically realistic, may in computation present too narrow a source width compared to the horizontal grid size. Bearing in mind that the largest grid size for T2 is 7 km, it is reasonable to choose a value larger than 30 km in order to prevent excessive numerical dispersion due to poor wave resolution. It can be shown from the results of Simanjuntak and Greenslade (2011), that for the range of widths presented above, a width discrepancy of 20 km would produce a bias that is less than 13%. For a typical $M_w = 7.0$ tsunami entering the Australian coastal zones, this bias translates to less than 0.5 cm.

From the above considerations and discussions within the JATWC, the final decision on rupture dimensions is as shown in the first row of Table 1, i.e. $W = 35$ km, $L = 50$ km, and $u_o = 0.5$ m. Other factors, such as dip and strike are a direct function of the location. The depth of the top of the rupture is fixed at 10 km, as for all the other T2 scenarios.

Locations of Rupture Elements

The epicentres of the existing T2 scenarios have been specified so that the mid-points of the top edges of the ruptures are coincident for all scenarios of any magnitude at a particular location. This means that the $M_w = 7.5$ scenarios are staggered relative to the locations of the rupture elements of the other magnitude scenarios (see Figure 3 in Greenslade et al., 2009). An obvious positioning for the $M_w = 7.0$

scenarios is to have the central points of the top edges of the ruptures coinciding with those of the $M_w = 7.5$ scenarios. The distance between the centroids of these ruptures is 100 km, with rupture lengths of 100 km and there are 521 of them throughout the entire Indian and Pacific Oceans.

As discussed above, the $M_w = 7.0$ ruptures have lengths of less than 100 km, so this means that if they are located co-incident with the $M_w = 7.5$ scenarios, the ruptures will be ‘non-contiguous’ and there will be gaps of 50 km between each rupture. Alternative solutions could be to either define the $M_w = 7.0$ scenarios with longer ruptures to reduce the gaps, or to define new epicentres which are a distance L apart, so that the ruptures are contiguous. Making the ruptures contiguous will necessitate the creation of scenarios with ‘non-orthodox’ epicentres, which will cause complications in the existing scenario numbering scheme and will require considerably greater computing resources (in terms of both computation and storage). Although non-contiguous ruptures may cause issues with scenario selection during an event, the epicentre of an event will never be more than 50 km away (along the strike) from the closest scenario. Therefore, the $M_w = 7.0$ scenarios have been generated with epicentres at the same locations as the $M_w = 7.5$ scenarios, and the gaps between the ruptures will be tolerated.

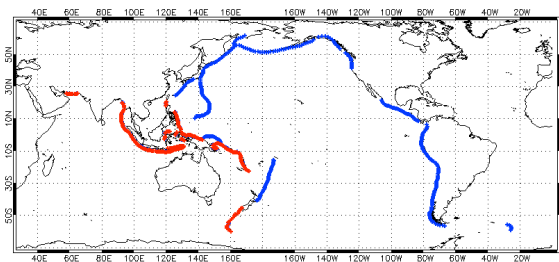


Figure 2 T2 domain and rupture locations. The locations of epicentres of the $M_w = 7.0$ scenarios are shown in red.

The 203 locations of the epicentres of the $M_w = 7.0$ scenarios are shown in Figure 2. These locations are those that are a) within the Indian Ocean and/or b) likely to affect Australia.

(a)

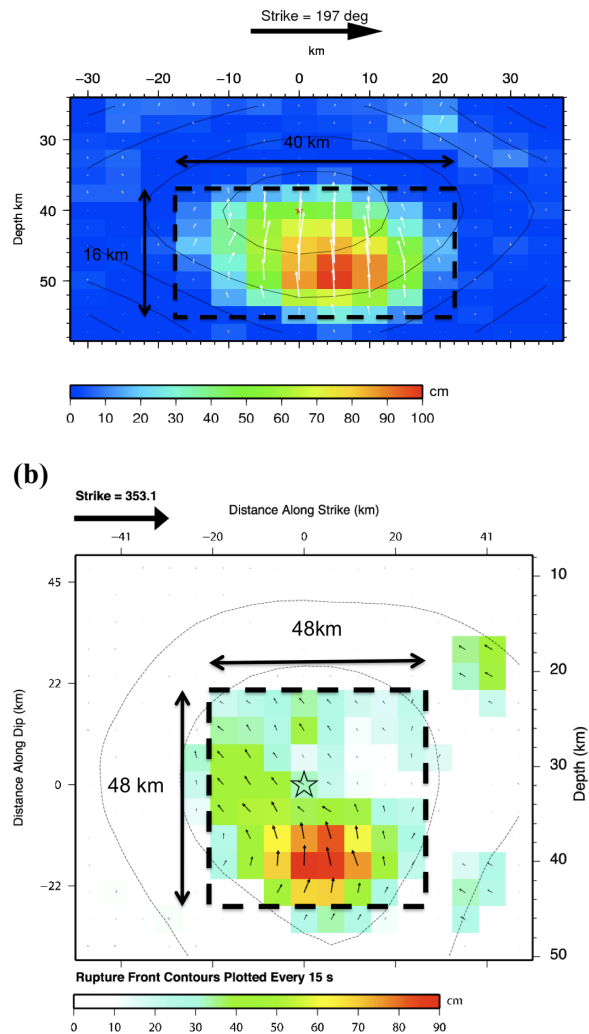


Figure 3 Slip distributions for the (a) 2008 Kermadec earthquake (reproduced from Hayes, 2008) and (b) 2011 Vanuatu earthquakes (reproduced from Hayes, 2011a). We have added dashed rectangles and the rulers delineating ideal rupture boundaries.

Verification

Ideally, these scenarios would be verified against observational data. There are very few observations of tsunami waves from tsunami buoys for earthquakes below $M_w = 7.5$. Tsunami amplitudes from these events are typically less than 1cm, which is too small to warrant a reliable comparison with the numerical model. In the absence of the possibility of verifying the tsunami sea-level, we compare the rupture characteristics from the new scenarios to slip distributions from finite fault analyses of previous earthquakes. These are taken from the

USGS database¹. From 2004 to 2011, there are only two $M_w < 7.5$ tsunamigenic earthquakes within the south east Pacific region for which finite fault analyses are available. These are the 29 September 2008 M_w 7.0 earthquake along the Kermadec fault, and the 20 August 2011 M_w 7.1 earthquake off Vanuatu. Notice that the latter event occurred after the $M_w = 7.0$ scenarios were completed.

Figures 3a and b show the slip distributions for the 2008 Kermadec and 2011 Vanuatu earthquakes, respectively. Inspection of these Figures suggests rupture lengths of approximately 50 km. The vertical axis in Figure 3(a) is the depth, whereas that of Figure 3(b) is the distance along the dip (which is the definition of rupture width in T2). For conversion to width, depth must be multiplied by the reciprocal of the sine of the dip angle. For dip angle of 30 degrees for the Kermadec event (Hayes 2008), the delineated depth of 16 km (Figure 3a) translates to width of 32 km. The average slip values for the ruptures (defined by the area where slip is greater than 10 cm) were calculated to be 35 cm and 50 cm, respectively. These values are similar to the chosen dimensions of the new $M_w = 7.0$ scenarios, confirming that these are reasonable choices.

Magnitude 9.0 Puysegur scenario

Within the T2 scenario database, $M_w = 9.0$ scenarios have only been generated on subduction zones that could support ruptures of 1000 km length (with the exception of the South Sandwich subduction zone). This 1000 km rupture length was based loosely on the Indian Ocean event of 2004. The Puysegur subduction zone, south of New Zealand, is only ~600 km long (Bird, 2003) and so was not deemed capable of supporting a $M_w = 9.0$ earthquake. Until now, the highest magnitude scenario in this region was a $M_w = 8.5$, which could be appropriately scaled to provide guidance for earthquakes of M_w up to 8.7.

The JATWC recently requested numerical guidance for larger earthquakes in this area. Furthermore recent large events have

demonstrated that very large earthquakes can be generated with ruptures significantly shorter than 1000 km. The Chile 2010 event (Hayes, 2010) was $M_w = 8.8$ and had a rupture length of approximately 400 km and the Japan 2011 event was $M_w = 9.0$ with a rupture length of approximately 300 km (Hayes, 2011b). It therefore seems prudent to provide numerical guidance for a $M_w = 9.0$ on the Puysegur subduction zone. This has been done, and the rupture details for this are shown in Table 1.

Summary

A total of 204 new scenarios have recently been added to the T2 scenario database, consisting of 203 $M_w = 7.0$ simulations and one $M_w = 9.0$ simulation. The rupture dimensions for these new scenarios are shown in the blue shaded areas in Table 1.

An obvious advantage of having $M_w = 7.0$ scenarios in the T2 database is that numerical guidance for tsunamis generated by earthquakes of M_w less than 7.3 can now be scaled from the nearest $M_w = 7.0$ scenario instead of the $M_w = 7.5$ scenarios. The extended T2 scenario database now consists of 2,069 scenarios and, with appropriate scaling, can provide guidance for any earthquake from $M_w = 6.8$ to $M_w = 9.3$ in the Indian Ocean and south-west Pacific, and $M_w = 7.3$ to 9.2 elsewhere.

References

- Bird, 2003. An updated digital model of plate boundaries. *Geochemistry Geophysics Geosystems* 4(3)
- Greenslade, D.J.M., Simanjuntak, M.A., and Allen, S.C.R. (2009). An enhanced tsunami scenario database: T2. *CAWCR Technical Report* 14(8).
- Hanks, T.C. and Kanamori, H. (1979). A Moment Magnitude Scale. *Journal of Geophysical Research* 84(B5), 2348-2350
- Hayes, G. (2008) Finite Fault Model Preliminary Result of the Sep 29, 2008 Mw 7.0 Kermadec Islands Earthquake, web document.
http://earthquake.usgs.gov/earthquakes/eqinthenews/2008/us2008xna6/finite_fault.php
- Hayes, G. (2010). Updated Result of the Feb 27, 2010 Mw 8.8 Maule, Chile Earthquake, web document.
http://earthquake.usgs.gov/earthquakes/eqinthenews/2010/us2010tfan/finite_fault.php

Hayes, G. (2011a) Finite Fault Model Preliminary Result of

¹ <http://earthquake.usgs.gov/earthquakes/world/historical.php>

the Aug 20, 2011 Mw 7.1 Vanuatu Earthquake, web document:

http://earthquake.usgs.gov/earthquakes/eqinthenews/2011/usc0005h9f/finite_fault.php

Hayes, G. (2011b). Updated Result of the Mar 11, 2011 Mw 9.0 Earthquake Offshore Honshu, Japan, web document:

http://earthquake.usgs.gov/earthquakes/eqinthenews/2011/usc0001xgp/finite_fault.php

Joint Australian Tsunami Warning Centre (2011), RTSP User Services Guide for National Tsunami Warning Centres, Bureau of Meteorology, unpublished document.

Pacheco, J.F., Sykes, L.R. and Scholz, C.H. 1993. Nature of seismic coupling along simple plate boundaries of the subduction type. *J. Geophys. Res.*, 98 (B8), 14,133–14,159.

Simanjuntak, M.A. and Greenslade, D.J.M. (2011). Magnitude-based scaling of tsunami propagation". *Journal of Geophysical Research* 116(C7).

Wells, D.L. and Coppersmith, K.J. 1994. New empirical relationships among magnitude, rupture length, rupture width, rupture area and surface displacement. *Bull. Seism. Soc., Amer.*, 84 (4), 974–1002.

Evaluation of simulated Australian climate for the Hadley Centre's CAPTIVATE Project

Ian G. Watterson, Anthony C. Hirst and Arnold Sullivan

CAWCR, Aspendale, Victoria

Ian.Watterson@csiro.au

Introduction

In the past five years, CAWCR has been developing the new ACCESS coupled climate model, which uses as its atmospheric component the Met Office's Unified Model (UM). Over this time, the Model Evaluation group in the Earth System Modelling Program has developed methods for objectively assessing the performance of the model. In late 2010 the group accepted an invitation to join the Met Office Hadley Centre's project 'CAPTIVATE' (standing for Climate Processes, Variability and Teleconnections), which aims to evaluate the simulation of climate processes in successive versions of the Hadley Centre's new coupled climate model, HadGEM3, that also incorporates the UM. CAPTIVATE comprised a development and evaluation cycle featuring rounds of assessment of standardised and internally documented model versions at 6-monthly intervals. The CAWCR task was to perform evaluations for the Australian region, on both coupled and atmosphere/land-only versions of HadGEM3, using the Hadley Centre's preceding model, HadGEM2, as the 'Reference' to which the HadGEM3 solutions are to be compared. CAWCR was involved in two rounds of assessment, for model simulations performed around September 2010 and March 2011, prior to the completion of the project. The final report, Scaife et al. (2011), includes a summary of various global and regional assessments, including that for Australia in 'traffic light' form. Similar evaluations have been made on preliminary versions of ACCESS as reported in brief by Watterson (2011b).

The main purpose of this paper is to present the assessment method in some detail. We describe tests targeting features of the mean state climatology (CLIM), variability (VAR) and teleconnections (TELE) that are important to

Australian climate. The tests are applied here to the Hadley Centre simulations of the present-day climate for the CAPTIVATE project, described in the next section. Application to ACCESS will be reported in due course. The assessment of the variability and teleconnection focuses on Australian rainfall and its 'drivers', specifically tropical SST anomalies and atmospheric circulations, represented in novel ways. The observational results are of considerable interest in their own right.

CAPTIVATE Models

The Reference model (denoted 'Ref' in Table 1 along with the code names of the specific runs analysed) is the HadGEM2-AO (coupled) and HadGEM2-A (atmosphere/land) model as described by HadGEM2 Development Team: Martin et al. (2011). The atmospheric component is the HadGEM2 r1.1 atmosphere based on the UM version 6.6.3, with resolution denoted N96L38, with a grid spacing of 1.25° latitude and 1.875° longitude, and with 38 levels in the vertical. The MOSES land surface model is used and the ocean and sea ice codes are directly coupled to the atmosphere. The ocean resolution is 1° latitude/longitude with additional refinement in the tropics.

The standard HadGEM3 model versions evaluated for both rounds have atmospheric components again with N96 horizontal resolution, but with higher vertical resolution (85 levels) and a revised atmospheric configuration (GA2.0, vn7.6 for round 1; GA3.0, vn7.7 for round 2 – see Walters et al. 2011). The JULES land surface model (Best et al. 2011) is used. The coupled model uses the CICE sea-ice model (Hunke and Lipscombe, 2008), OASIS coupler (Valcke, 2006) and the ORCA configuration of the NEMO ocean model (Madec 2011), on a tripolar grid with nominal

resolution 1°, and with additional refinement in the tropics. . Hewitt et al. (2011) describe the technical infrastructure of the coupled model, together with the specifics of the CICE and NEMO implementations. A HadGEM3 version with higher horizontal resolution (suffix ‘H’) was also assessed for the second round, having an N216 grid for the atmosphere (0.55° lat. by 0.83° lon.) and the ORCA 0.25° ocean. A coupled and an atmosphere/land-only simulation are performed for each version. The later follow the ‘AMIP’ experimental procedure, run for the period 1979-2008 with specified observed monthly sea surface temperature (SST) and sea ice extent, and are denoted suffix ‘A’.

Details of the configurations used can be found in Walters et al. (2011) and Scaife et al. (2011). During the project changes were made to the parameterisations of convective cloud, light rain, and boundary layer physics. These targeted biases in the North Atlantic storms tracks, Indian monsoon, ENSO and Southern Ocean temperatures. The changes were not specific to Australian climate, but may influence it. The simulations assessed in the ‘Round 1’ (or R1) and ‘Round 2’ (R2) assessments are listed in Table 1. Model data length was less than ideal with 30-y means used for the CLIM tests. For VAR/TELE 50-y monthly series were available for the three fields used, except for R2 (only 26 y).

For an initial look at the model climate for Australia, we include the overall means of surface air temperature ‘T’ and precipitation ‘Ppn’ in Table 1. These can be compared to the observational averages of Bureau of Meteorology (BoM) gridded (0.25°) monthly fields averaged over 1958-2001 (matching the period of the ERA-40 reanalysis data). The BoM T is the average of the daily maximum and minimum fields. A second data set is the ERA-Interim reanalysis (1.5° grid) over 1989-2008. All model results are within 1°C or 0.3 mm/d of one of the ‘obs’. The R2 (coupled) model is an improvement on R1, and marginally on Ref. The R2H version is closer to the average of obs. Interestingly, while the A versions have little variation in temperature, as expected from the constrained SSTs, there is a wider range for Ppn than in the coupled models.

Maps of the Ppn fields from BoM and five versions are shown in Figure 1. All models simulate the basic pattern. R2H has the closest match to the dryness in the centre, but is too dry in the northeast. Rainfall along the wetter coasts, including the southwest, tends to be too light. The two H versions begin to resolve the orographic enhancement in the southeast.

Table 1 CAPTIVATE model versions (see text) and the run name, together with their Australian mean temperature and rainfall. The first four entries are coupled models. The atmosphere/land-only models are indicated by ‘A’, and high-resolution by ‘H’. Observational data from two sources also given.

Model	Run	T °C	Ppn mm/d
Ref	ajpdr	21.31	1.23
R1	ajtzd	23.11	1.64
R2	ajtzt	22.36	1.39
R2H	xfhkk	22.28	1.22
RefA	ajhbc	22.45	0.90
R1A	ajrih	22.27	1.47
R2A	akkvi	22.79	1.11
R2AH	ajthm	22.57	1.35
obs	BoM	21.84	1.36
obs	ERA-Int	22.12	1.17

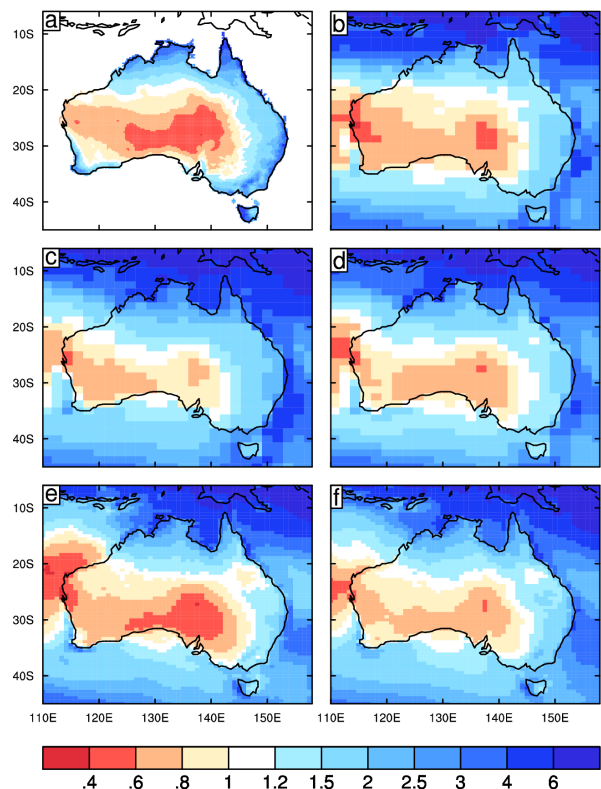


Figure 1 Annual precipitation (in mm/d) for the Australian region. The BoM observations are shown as (a), along with four coupled model fields, (b) Ref, (c) R1, (d) R2, (e) R2H, and the AMIP (f) R2AH.

Climatology Tests ‘CLIM’

The Australian summary chart includes, under CLIM, assessment of T, Ppn and seven features of atmospheric circulation (Table 2). Restricting the test to seasonal climatologies of available variables meant that features such as ‘monsoon onset’ could only be assessed in a very approximate way. A further simplification was the testing of only spatial fields over suitable domains, using the non-dimension metric ‘M’.

For the model field X and observed field Y, this statistic of agreement is given by

$$M = 1000 \times (2/\pi) \arcsin[1 - mse / (V_X + V_Y + (G_X - G_Y)^2)],$$

with *mse* the mean square error between the model field X and observed field Y, and V and G are variance and domain mean of the fields (as subscripted, see Watterson et al., 1999 for details). Using *M* allowed scores for different variables and seasons to be averaged.

The four domains used are:

Aust land,
Region 105-165°E, 50-0°S;
Monsoon Onset 120-150°E, 20-10°S;
SubTropical Jet 140-150°E, 40-15°S.

The variables (using the CMIP5 names) and domains for each test are given in Table 2. All four standard seasons were used, except for monsoon onset, for which September-November

and December-February results were averaged.

Two observational datasets are used in each test. These differ by source and averaging period. Comparing the secondary set (obs2) with the primary set (obs1) provides some indication of the value of a metric that a ‘near-perfect’ model might be able to attain. For most quantities, the primary set is from the ERA-Interim reanalyses, (as above, but with January-February 2009 also used in the DJF case). The secondary set is from ERA-40 (2.5° grid). For the tests T and Ppn, obs1 is from BoM (as before), and ERA-Interim is obs2.

The scores for Obs2 (versus Obs1) are mostly above 850, which indicates strong similarity between these data sets. For Ppn, however, there is considerable differences between the data sets. The model results score mostly around 700-800 for the dynamical fields, and 600 for Ppn. Generally the A cases score a little better than the coupled cases, as expected, though only for T and 500GPH does the RefA case do better than Ref. The R1A and R2A cases have improved on RefA. In some cases, the high resolution model has an improved score, but these tests have little sensitivity to small details (such as those seen in Figure 1).

Table 2 CLIM tests for ten features, with variables and domain given, followed by scores for Obs2 and eight models, compared with Obs1. The colour grades are indicated. Note that swapping rows and columns might be helpful to match other tables.

Feature	Fields- CMIP5 name	Domain	obs2	Ref	R1	R2	R2H	RefA	R1A	R2A	R2AH
1.5m T	tas	Aust	875	810	720	770	816	821	827	789	830
850wind	ua, va 850hPa	Reg	887	727	749	764	774	747	795	803	816
200wind	ua, va 200hPa	Reg	903	747	772	714	735	656	780	760	786
SLP	psl	Reg	948	800	750	760	739	805	830	816	793
500GPH	zg 500hPa	Reg	973	892	917	890	900	933	928	933	934
10m wind	uas, vas	Aust	809	768	737	742	757	736	771	761	772
Ppn	pr	Aust	690	573	613	567	580	489	601	546	619
Mons. Ons.	uas, vas ua 925hPa	N. Aust	909	724	711	725	761	717	768	773	762
SubTJet	ua, 925, 850, 250, 200 hPa	E. Aust	941	804	769	751	821	781	790	839	811

Overall the R1 and R2 coupled models give rather similar results to Ref. This is made clearer using the colour grades applied to the scores, as follows:

Green av of Obs2, 850
 Yellow > Ref +10
 Amber within Ref \pm 10
 Red < Ref -10.

The criterion for Green, which is ideally ‘fit for purpose’ is subjective. It is evident from Table 2 that for the Australian features the new *coupled* versions have not improved on Ref overall despite the higher resolution of HadGEM3. The improvement in the A cases is encouraging, nevertheless.

Variability and Teleconnection

The summary chart includes under VAR/TELE a range of features such as those depicted and assessed by Risbey et al. (2009). Given the time and data limitations, and the need to examine both observations and multiple models, it was decided to assess only seasonal and regional rainfall and several drivers of variability. Furthermore only the Ref, R1 and R2 models were assessed.

Time series of rainfall are readily available from the BoM website for seven key regions, as listed in Table 3. Some of the detail in rainfall patterns is lost by this choice, but the standard resolution global models are not expected to simulate this. The first region is the all-Australia average (All), and clearly there is some overlapping of regions. Two regions are ‘north’ (Nth) and ‘south’ (Sth), divided by the latitude 26°S. The eastern region is the four eastern states (in a model this is simplified to be east of 141°E). The southeastern (SE) region is south of 33°S and east of 135°E (see Figure 2, for the region as represented by an N96 model). Southwestern (SW) is the far southwest of WA (in a model, the land bounded by 115-120°E, 35°S-31°S). The Murray Darling Basin (MDB) is the seventh region, simplified to 139-150°E, 37-25°S.

Likewise, we represent drivers only in a coarse way. Watterson (2011a) argued that the gradient of SSTs from the north-west to north-east of Australia is a basic feature that models should simulate. This is quantified by a Pacific (minus) Indian Dipole index (PID). Analysis has shown

that this is closely related to the more commonly studied ENSO and Indian Ocean Dipole (IOD) indices, though, for the annual case, PID displays similar or higher correlations with the regional rainfall series. Tests indicate that stronger correlations are obtained with the Indian Ocean region extended to the north of Australia, with the band becoming 15°S-5°N, 85-135°E (Figure 2). The Pacific region remains 10°S-10°N, 150-200°E. Averages of T over ocean points in each domain are taken, and the simple difference forms PID, with unit K.

Atmospheric circulation features that drive rainfall are here limited to a sectoral SAM (southern annular mode) or ‘high latitude mode’ HLM and two sub-domain blocking indices (BIs). All three are formed from box averages of the zonal wind (ua) at 500 hPa. HLM is based on longitudes 80-170°E, and the box over 60-55°S minus that over 40-35°S (see Figure 2). For the BIs, the longitude spans are 135-155°E (east BI or EBI) and 110-130°E (WBI). In each case, the latitudes of the boxes are over 50-45°S and 30-25°S, and again the index is simply the southern value minus the northern value.

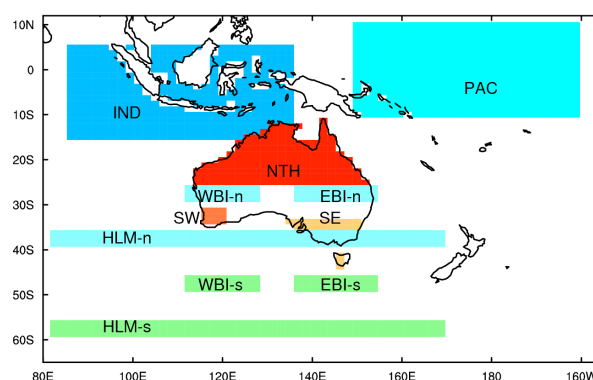


Figure 2 Some regions used in the assessment, on the model grid. Three Australian land regions are shown (SE, SW and NTH). The tropical ocean regions (PAC, IND) are used for PID. The regions for the wind indices HLM, EBI and WBI (on the surface grid) are plotted, with s and n denoted the southern and northern components. SE extends under HLM-n.

The EBI should relate especially to southeastern regions, while the WBI relates to the southwest. For simplicity, all the tests use time series of yearly values of area averages, of either annual (calendar years) or seasonal means (of three consecutive months).

Variability Assessment (VAR)

In our VAR tests we consider the variability of the rainfall (Ppn, in seven regions) and the four indices (PID, HLM, EBI and WBI) in each of five seasons (counting annual mean as one). Naturally, there is overlap in the time period, as in the regions, but ultimately we need a single objective grade in all these tests!

The only statistic used is the standard deviation (SD) of each series. For rainfall, we consider the SD as a percentage of the mean rainfall. The magnitude of the difference in model SD from the observational SD is a basic bias measure. To focus on the contribution from year-to-year variability the SD is calculated from detrended indices. Detrending removes part of the variation forced through global warming (although this is less linear before 1950). In model runs, some (linear) climate drift may occur, and this is removed.

Observational results

The BoM Australian series for 1900-2010 are used (with 111 yearly values, including summer, which includes Jan-Feb of 2011). For reference, the mean for each region is given in Table 3, for the annual case. The SD ranges from 16% (SW) to 24% (MDB) as a percentage of the mean in the annual case (Table 3). The peak values among the four seasons feature in Table 4. Except for the SE and SW, with a peak in winter, there is generally more rain in summer. Variability as a percentage peaks in different seasons, depending on the region. It tends to be largest in the driest season. The average of the SD values, over all 35 cases, is given in Table 5. For SST, the HadISST data (1° grid) over 1950-2010 are used (plus Dec 1949). This provides 61

yearly values, for both the SD and the correlation with rain. The average of the SD values (5 cases) is 0.35 K (Table 5). For the wind indices, reanalysis data over 1957-2010 are used. Over 1989-2010, ERA-interim is used, and prior to that ERA-40. In the dozen years of overlap between these two reanalysis sets, the values are closely related – nevertheless any bias in the time mean (including that due to the different grids) in that period is added to the earlier ERA-40 data. Interestingly, the average SD for HLM is quite close to that of the two BIs combined (Table 5).

Table 3 Observed annual statistics, for the seven rainfall regions. Shown are the mean and SD of rainfall, and the correlation of annual values with those of the four driver indices. These are HLM (a sectoral SAM), EBI eastern blocking index, WBI western blocking index, PID (SST index, Pacific-Indian Dipole).

	Ppn Mean mm/d	Ppn SD (%)	HLM r x 100	EBI r x 100	WBI r x 100	PID r x 100
All	1.24	17	16	-9	11	-55
East	1.67	21	18	-22	-4	-63
Nth	1.41	20	10	5	25	-45
Sth	1.05	17	23	-33	-17	-64
SE	1.72	17	7	-51	-33	-55
SW	1.86	16	-19	-21	-39	-28
MDB	1.29	24	26	-30	-15	-63

Table 4 Observed seasonal statistics, for the seven rainfall regions and their drivers (as in Table 3). The season with largest magnitude result is indicated, along with the result. Code S summer, A autumn, W winter, P spring.

	Ppn Mean mm/d	Ppn SD (%)	HLM r x 100	EBI r x 100	WBI r x 100	PID r x 100
All	S 2.31	P 37	P 26	S 47	S 47	P-76
East	S 2.92	P 39	P 26	W -34	S 32	P-69
Nth	S 3.33	W 57	W 21	S 50	S 51	P-77
Sth	S 1.14	A 33	S 43	W -48	W-54	P-67
SE	W 2.06	S 33	S 37	W -68	W-67	P-58
SW	W 3.62	S 67	W-36	P -37	W-61	P-24
MDB	S 1.56	A 48	S 37	W -41	W-39	P-61

Table 5 Variability (VAR) of rainfall and of indices from obs and models, including mean bias. In each case the result is an average over the five seasons (including annual). The rainfall is given as a percentage of the mean, and the average is over the seven regions as well. For BI, the average is over the EBI and WBI. The bias is calculated by averaging the absolute differences from the obs results.

	Ppn SD %	Ppn bias %	HLM SD m/s	HLM bias m/s	BI SD m/s	BI bias m/s	PID SD K	PID bias K
obs	31.3	0.0	3.45	0.0	3.34	0.0	0.353	0.0
Ref	31.7	4.2	3.76	0.40	3.26	0.44	0.294	0.059
R1	30.6	5.2	3.92	0.67	3.23	0.58	0.495	0.141
R2	29.7	6.9	4.58	1.14	3.38	0.52	0.241	0.113

The corresponding rainfall and driver time series have been calculated from the three models considered here. While individual results would be of interest, for brevity we present only the averages, starting with the SDs, given in Table 5. The overall variability of rainfall, as a percentage, is remarkably well matched by the Ref model, as well as R1 and R2. Note though that larger SDs (in %) for the SW region, which is drier than observed (see Figure 1), tend to compensate for smaller SD in some other regions. Overall variability in the wind indices is also quite realistic, while the PID is more variable than observed in R1 but less in R2.

The score statistic is simply the magnitude of the difference between the model SD and the obs SD (or ‘bias’), for each case. We could consider only the larger values, but, as with TELE, it seems also important that the model produce small values, when they occur in obs. For our single grade we average over all cases, and assign colours. Without an objective target for Green, we take the criterion value to be simply half the largest of the three results. (For the initial report an additional ACCESS case was included, but the grades are unchanged by its omission.) For Amber, the mean difference is to be within 20% of the Ref result, allowing for statistical uncertainty in both obs and model SDs. This criterion is again subjective, but is rather consistent with the range of values found when assessing different 50-year periods from longer ACCESS runs.

The final scores and the colour grades are given in Table 5. For Ref, the average bias is within 17% of the average SD in each quantity. Given that statistical uncertainty will produce positive bias for each case, this seems excellent. Two scores are rated Green here. Both R1 and R2 have somewhat less success in each category (with only one Amber). With only 26 years of

data for R2, we should expect that its results are degraded by chance. Still, there is no improvement over Ref evident, and little over R1.

Teleconnection Assessment (TELE)

The TELE section focuses on the links between these drivers and rainfall. The statistic is the correlation r between each pair of detrended series. Only the contemporaneous (zero time lag) relationship is considered. With 50 yearly values in most cases, correlations need only be 0.2 or so to be of statistical significance. We need not focus on this, given that values would need to be larger to be of practical significance, but uncertainty is not ignored.

The observational results, calculated from coincident periods of the data, are of particular interest. The correlation between each regional series and the annual series of each index is then shown in Table 3. The HLM wind index is positively correlated, except for the SW. This might be expected from previous results for the (all-longitude) SAM (e.g., Risbey et al., 2009), given that the drying associated with higher SAM is mostly seen in the far south and in winter. Enhanced easterlies further north tend to raise rainfall over much of the continent. The largest magnitude seasonal correlations are given in Table 4. The SW value for HLM is more strongly negative in winter, while the positive cases are stronger in summer. The average magnitude of the correlation, given in Table 5, is rather small, particularly considering statistical uncertainty.

Correlations for the BIs are mostly negative (Tables 3 and 4). They tend to be larger in the southern regions, for the index most adjacent (in longitude), and also in winter. The peaks of -0.7 seem typical of values in other studies. Substantial positive values occur in summer for

the north. Conceivably, these are ‘coincidental’ with both the northern rainfall and the wind anomalies (well to the south) being part of an ENSO teleconnection.

For all the regions there is a negative correlation with the PID index. Except for SW it is substantial, both in the annual case and the seasons. (An exception is in summer, when the east-west gradient here seems less important than the variation in overall equatorial temperatures associated with ENSO.) In each case, the peak seasonal value is in spring, which also has the largest SD of PID. The average of the *r* values, in Table 6, is notably large, indicating the overall importance of this relationship.

Turning to the model results, we again present only the averages in Table 6 (and not just the large values). The HLM relationship is stronger in Ref than in the obs, and the average bias is also largest for Ref, despite it having the best VAR result. Using the same colour criteria as for VAR, we rate both R1 and R2 as improved, with Yellow.

Table 6 Teleconnection (TELE) between indices and rainfall from obs and models, using the correlation coefficient *r* (times 100), including the bias. In each case the result is an average over the five seasons (including annual) and seven rainfall regions. For the HLM and BI cases, the values are the average of the magnitude of *r*. For BI, the average is over the EBI and WBI. The bias is calculated by averaging the absolute differences from the obs results.

DATA	HLM-Ppn abs(r)x100	HLM-Ppn bias	BI-Ppn abs(r)	BI-Ppn bias	PID-Ppn r x100	PID-Ppn bias
obs	21	0.0	27	0.0	-42	0.0
Ref	39	24	25	16	-25	19
R1	22	14	29	16	-41	12
R2	27	13	28	17	-16	32

The two blocking indices also correlate rather modestly with rainfall overall, with similar

averages in each model (Table 6). The model bias in *r* is also similar in each case. As a result each model is given Amber.

The observed PID-rain relationship is most closely matched by the R1 model. The other two, including Ref, have both weaker correlations and a smaller SD of PID. They have larger overall bias in *r*, also. As a result the R2 is graded Red, while R1 scores Green. With the R1 PID being also more variable, but not its rainfall, it could be argued that the models have a somewhat weaker Australian rainfall response to PID, per K of the index.

Summary and Conclusions

We have presented and applied objective tests for nine features of climatology, four for the variability of rainfall and its drivers, and three for the associated teleconnections. Figure 3 shows summary charts for the analysis. The chart for the round 1 coupled model shown in Figure 3a, indicates a mostly negative comparison with the Reference model. Nine out of the 16 grades are Red. There is some improvement in TELE, at least. The R2 chart, Figure 3b, shows similar performance to R1.

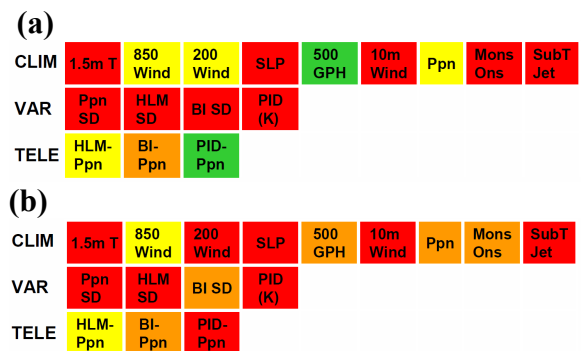


Figure 3 Australian regional summary charts for models (a) R1, and (b) R2.

Based on the charts, and the previous tables, it can be said that the round 2 models perform as well as round 1, for the climatology features in the Australian region. There is some improvement of the round 2 AMIP runs over the reference, but no clear change for the coupled model with the high resolution case better in some respects.

The regional rainfall averages are key indicators of Australian climate variability and the Hadley

Centre coupled models provide quite realistic results overall. The PID index of equatorial SST relates strongly to the rainfall variability, in both obs and the models although there is apparently less realism in the round 2 model. The wind indices, sectoral HLM and east and west blocking indices provide an indication of the variability of the tropospheric zonal winds in the Australian sector. The models simulate a similar amount of variability overall and it relates well to the rainfall.

Looking over both VAR and TELE features, the scores for round 1 and round 2 have not reached the impressive level set by the reference model. However, these are only initial results, and the data sets, particularly from the round 2 model, are rather limited. The grades and indeed the method are presented here for consideration, and should not be regarded as conclusive.

To conclude, these tests assess model performance in the Australian region for a range of features, from climatology, variability and teleconnections. Substantial refinement of some of the tests is warranted, in particular via further quantification of error in the observational data sets and via usage of longer time series at finer temporal resolution (e.g., monthly). While the tests oversimplify some aspects and overlook some of the detail that may be important locally, they are practical enough to apply on a routine basis to new versions and other models, in particular ACCESS.

Acknowledgements

The CAPTIVATE project has been led by Adam Scaife (Met Office). We thank the modellers at both the Hadley Centre and within CAWCR for the opportunity to analyse data from their developmental models. The CAWCR Earth Systems Modelling Program's Model Evaluation Team, led by Lawrie Rikus, has given ongoing support to this work. Charline Manzin (Met Office) provided the Hadley Centre data and much advice. Lawrie Rikus and Harun Rashid provided helpful comments on the manuscript.

References

Best, M. J., Pryor, M., Clark, D. B., Rooney, G. G., Essery, R. L. H., M'Enard, C. B., Edwards, J. M., Hendry, M. A., Porson, A., Gedney, N., Mercado, L. M., Sitch, S., Blyth, E., Boucher, O., Cox, P. M., Grimmond, C. S. B., and

Harding, R. J., 2011: The Joint UK Land Environment Simulator (JULES), Model description – Part 1: Energy and water fluxes, *Geosci. Model Dev.*, 4, 677–699.

HadGEM2 Development Team: Martin, G. M., Bellouin, N., Collins, W. J., Culverwell, I. D., Halloran, P. R., Hardiman, S. C., Hinton, T. J., Jones, C. D., McDonald, R. E., McLaren, A. J., O'Connor, F. M., Roberts, M. J., Rodriguez, J. M., Woodward, S., Best, M. J., Brooks, M. E., Brown, A. R., Butchart, N., Dearden, C., Derbyshire, S. H., Dharssi, I., Doutriaux-Boucher, M., Edwards, J. M., Falloon, P. D., Gedney, N., Gray, L. J., Hewitt, H. T., Hobson, M., Huddleston, M. R., Hughes, J., Ineson, S., Ingram, W. J., James, P. M., Johns, T. C., Johnson, C. E., Jones, A., Jones, C. P., Joshi, M. M., Keen, A. B., Liddicoat, S., Lock, A. P., Maidens, A. V., Manners, J. C., Milton, S. F., Rae, J. G. L., Ridley, J. K., Sellar, A., Senior, C. A., Totterdell, I. J., Verhoef, A., Vidale, P. L., and Wiltshire, A., 2011: The HadGEM2 family of Met Office Unified Model climate configurations, *Geosci. Model Dev.*, 4, 723–757, doi:10.5194/gmd-4-723-2011.

Hewitt, H. T., Copsey, D., Culverwell, I. D., Harris, C. M., Hill, R. S. R., Keen, A. B., McLaren, A. J., and Hunke, E. C., 2011: Design and implementation of the infrastructure of HadGEM3: the next-generation Met Office climate modelling system, *Geosci. Model Dev.*, 4, 223–253.

Hunke, E. C. and Lipscombe, W. H., 2008: CICE: the Los Alamos sea ice model documentation and software user's manual, Version 4.0, LA-CC-06-012, Los Alamos National Laboratory, New Mexico.

Madec, G., 2008: NEMO ocean engine, Institut Pierre-Simon Laplace (IPSL), France, No. 27, ISSN No. 1288–1619.

Risbey, J. S., M. J. Pook, P. C. McIntosh, M. C. Wheeler and H. H. Hendon, 2009: On the Remote Drivers of Rainfall Variability in Australia. *Mon. Wea. Rev.* 137, 3233–3253

Adam Scaife A. A., Copsey, D., Kendon, L., Vidale, P.-L., Martin, G. M., Milton, S., Moufouma-Okia, W., Roberts, M. J., Palmer, Walters, D. N., and Williams, K., 2011: Final Report of the CAPTIVATE model development project. Deliverable D3.2.7 (Internal Report), Met. Office Hadley Centre.

Valcke, S.: OASIS3 user guide (prism 2-5), Tech. Rep. 3, Programme for integrated earth system modelling (PRISM) support initiative, 2006.

Walters, D. N., Best, M. J., Bushell, A. C., Copsey, D., Edwards, J. M., Falloon, P. D., Harris, C. M., Lock, A. P., Manners, J. C., Morcrette, C. J., Roberts, M. J., Stratton, R. A., Webster, S., Wilkinson, J. M., Willett, M. R., Boutle, I. A., Earnshaw, P. D., Hill, P. G., MacLachlan, C., Martin, G. M., Moufouma-Okia, W., Palmer, M. D., Petch, J. C., Rooney, G. G., Scaife, A. A., and Williams, K. D., 2011: The Met Office Unified Model Global Atmosphere 3.0/3.1 and JULES Global Land 3.0/3.1 configurations, *Geosci. Model Dev. Discuss.*, 4, 1213–1271.

Watterson, I. G., M.R. Dix and R.A. Colman, 1999: A comparison of present and doubled CO₂ climates and feedbacks simulated by three GCMs. *J. Geophys. Res.*, 104,

1943-1956

Watterson, I. G., 2011a: Understanding and partitioning future climates for Australian regions from CMIP3 using ocean warming indices. *Climatic Change*, doi:10.1007/s10584-011-0166-x

Watterson, I. G., 2011b: Evaluation of the ACCESS climate model for the CAPTIVATE Project. Abstracts of the Fifth International Verification Methods Workshop, 1-7 December 2011, Melbourne. CAWCR Technical Report No. 046, p53.